JOURNAL OF GEOPHYSICAL RESEARCH, VOL. 102, NO. B7, PAGES 15,163–15,182, JULY 10, 1997

The March 9, 1994 (M_W 7.6), deep Tonga earthquake: Rupture outside the seismically active slab

Jeffrey J. McGuire[1], Douglas A. Wiens, and Patrick J. Shore
Department of Earth and Planetary Sciences, Washington University, St. Louis, Missouri

Michael G. Bevis
Hawaii Institute of Geophysics, University of Hawaii, Honolulu

Abstract. We investigate the rupture process of the March 9, 1994, M_W 7.6 deep Tonga earthquake and its relationship to the background seismicity of the subducted Tonga slab. Variations in observed *P* and *S* wave pulse duration indicate that the rupture propagated to the NNE and extended well beyond the background seismicity. We inverted 47 *P* and *SH* waveforms, including regional broadband waveforms from the Southwest Pacific Seismic Experiment, using a method that solves for the focal mechanism change during the rupture and the distribution of moment release along the fault plane. The results indicate that significant moment release occurred in previously aseismic regions outside the active seismic zone and that the rupture terminated 10-20 km beyond the bounds of the previous seismic activity. A significant change in focal mechanism occurred when the rupture propagated into the previously aseismic region. Rupture along the near-vertical NNE striking nodal plane provides a somewhat better fit to the body waveforms than rupture along the near-horizontal nodal plane. This result, combined with the planar alignment of aftershocks and the general NNE directivity of the waveforms, provides strong evidence that the rupture occurred on the near-vertical plane. Thermal modeling of the Tonga slab indicates that the rupture terminated in material about 200°C warmer than the temperature that normally limits the occurrence of smaller earthquakes. Additionally, aftershocks seem to be suppressed in the outer regions of the rupture, which contain about half of the moment release but only 1 of the 15 well-located aftershocks. We suggest that slabs may be composed of an inner cold core, where seismic rupture initiates and small earthquakes occur, and a thermal "halo" of warmer material, which can sustain rupture and only a few aftershocks. The mechanism by which rupture propagates through the warmer material need not be similar to the process governing rupture nucleation in the cold slab core; nucleation may occur through a process limited to the cold core such as transformational faulting, and propagation through the warmer material may occur through ductile faulting or plastic instabilities. Isolated deep earthquakes in other subduction zones, such as the 1994 Bolivia event, may occur almost completely within the warmer zone, accounting for the lack of background seismicity and the dearth of aftershocks.

Introduction

The details of deep earthquake rupture, including the spatial extent and time history of the rupture and its relationship to the slab geometry defined by smaller earthquakes, are poorly known for most deep earthquakes. This is in part due to the absence of field evidence and significant aftershocks, which provide the strongest evidence for identification of the fault plane and rupture area for most shallow earthquakes. Previous large deep earthquakes have shown little to no aftershock activity, and what aftershocks did exist may not be located on either nodal plane [*Willemann and Frohlich*, 1987]. In addition, waveform inversion methods for determining deep earthquake rupture properties have not generally provided good resolution due to the generally small fault lengths of deep earthquakes and the absence of nearby stations, particularly since the largest deep earthquakes have occurred in relatively remote subduction zones.

A precise determination of the rupture area of a deep earthquake relative to the slab orientation and background seismicity is important for evaluating various models of the mechanism of deep earthquakes. Owing to the high-pressure conditions in deep earthquake source regions, it is unlikely that normal frictional failure can occur [*Leith and Sharpe*, 1936]. Thus the mechanism of deep earthquakes has been one of the fundamental problems in geophysics since their discovery [*Frohlich*, 1989; *Kirby et al.*, 1991]. Mechanisms that have been proposed for deep earthquakes include shear instability [*Ogawa*, 1987], transformational faulting due to the metastable olivine to spinel transformation [*Green and Burnley*, 1989; *Kirby et al.*, 1991] or the enstatite to ilmenite transformation [*Hogrefe et al.*, 1994], amorphization of serpentine [*Meade and Jeanloz*, 1991], and fluid-assisted failure on preexisting faults [*Silver et al.*, 1995]. These models are sensitive to the width and orientation of deep earthquake rupture areas because they predict either a stability field for a mineral like metastable olivine or a fault orientation such as trench parallel normal faults. A clear determination of the rupture area and orientation of a large deep

[1]Now at Department of Earth, Atmospheric, and Planetary Sciences, Massachusetts Institute of Technology, Cambridge.

Paper number 96JB03185
0148-0227/97/96JB-03185$09.00

earthquake relative to a deep seismogenic zone can provide strong constraints on the various mechanisms.

A number of authors have studied the rupture of various large deep earthquakes with various methods of waveform inversion [*Chung and Kanamori*, 1976; *Furumoto*, 1977; *Fukao and Kikuchi*, 1987; *Yoshida*, 1988; *Glennon and Chen*, 1995; *Kikuchi and Kanamori*, 1994; *Silver et al.*, 1995; *Beck et al.*, 1995]. In general, these studies have been able to suggest which of the two nodal planes represents the rupture plane, and they have been able to estimate the rupture area. However, the events with the largest magnitudes and greatest fault areas, such as the 1970 Columbia, 1954 Spanish, and 1994 Bolivia events, occurred in areas where the thickness and orientation of the seismogenic zone were not defined by previous seismicity. In the cases of moderate sized deep earthquakes in active slabs, the small size of the rupture inhibited the interpretation of the exact extent of seismogenic zone, or the ruptures studied were not considered in relation to the locations of smaller earthquakes in the area. In general, owing to the lack of aftershock activity and the tendency for large deep earthquakes to occur in regions of little to no seismicity [*Wiens and McGuire*, 1995], it has been hard to characterize the spatial extent of a large deep earthquake rupture relative to the subducting slab.

The March 9, 1994, Tonga Earthquake

The March 9th Tonga earthquake (M_W 7.6, depth 564 km) was larger than any deep earthquake in the previous 20 years and represents a unique opportunity to determine the orientation and spatial extent of a deep earthquake rupture area relative to the subducted lithosphere. The opportunity is enhanced because the March 9 event occurred beneath a temporary array of eight IRIS-PASSCAL (Incorporated Research Institutions for Seismology, Program for the Array Seismic Studies of the Continental Lithosphere) broadband seismometers [*Wiens et al.*, 1995] (Figure 1), giving excellent station coverage relative to typical deep earthquakes. We obtained seven on-scale *P* wave recordings and six on-scale *S* waves and both the *P* and *S* arrivals were recorded at the nearby IRIS permanent station AFI. Additionally, the March 9 event was unusually prolific in aftershock production relative to other large deep earthquakes, producing the strongest aftershock sequence ever recorded for a deep earthquake [*Wiens et al., 1994*]. The March 9th event is also ideally suited for studying the spatial relationship of the mainshock rupture to the seismically active slab since it is the largest deep earthquake recorded by modern instruments to occur in a highly seismic slab. The event occurred in a part of the subducted Pacific plate which is vertical, is relatively planar, and is well defined by the high amount of background seismicity.

The focal mechanism of the March 9 event shows a steeply dipping N-S striking nodal plane and a shallowly dipping E-W striking nodal plane. We inverted 20 teleseismic and 10 regional *P* and *SH* waveforms low pass filtered at 10 s to determine the

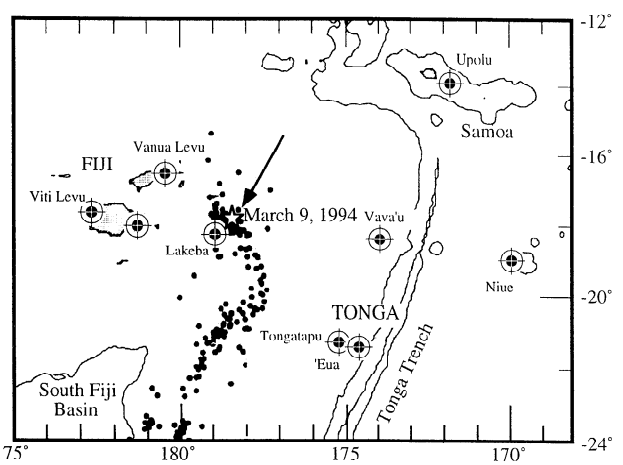

Figure 1. A map of the Fiji-Tonga region showing the location of the March 9, 1994, Tonga event (star), regional broadband stations of the Southwest Pacific Seismic Experiment (large solid dots with cross), and the permanent station AFI on Upolu, Samoa. The 4000 m and 8000 m bathymetric contours are shown, along with the locations of a 2-year sample of deep earthquakes in the Tonga slab (small solid dots). The arrow shows the strike of the steeply dipping fault plane of the March 9 event, as determined from the aftershock distribution.

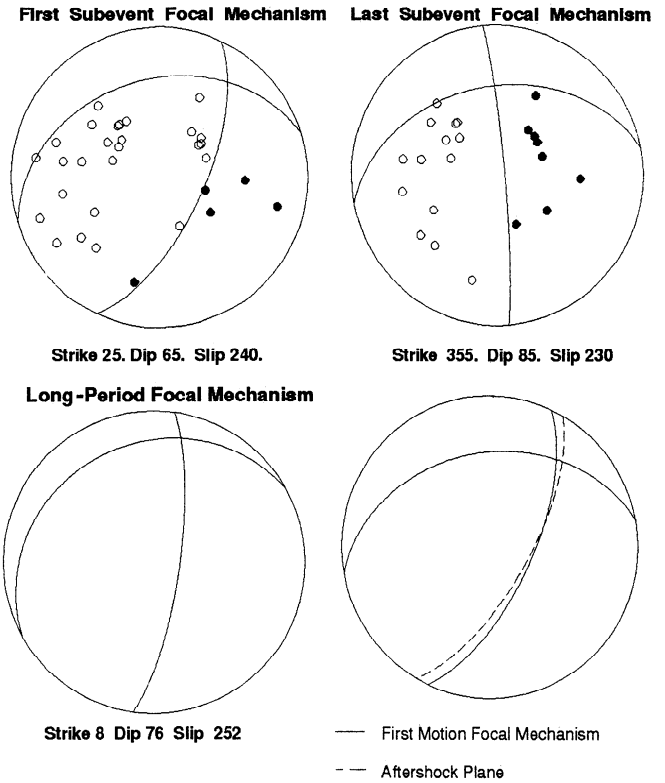

Figure 2. Focal mechanisms for the March 9 main shock. There was a large change in focal mechanism during the rupture, as illustrated by the focal mechanisms for the first (top left) and last (top right) subevents. The mechanisms for these subevents, determined by waveform inversion, are compatible with *P* wave polarities for the subevents determined from broadband displacement records. The difference between the focal mechanisms of the first and last subevents is clearly constrained by the polarity reversals observed for North American *P* waves. The long-period focal mechanism (lower left) was determined by inversion of long-period regional and teleseismic *P* and *SH* records and is nearly identical with the Harvard CMT solution. The long-period focal mechanism represents an approximate average between the first and last subevents. The lower right stereonet shows the focal mechanism for the first subevent (solid line) and the plane which is a least squares fit to the aftershock distribution (dashed line) [*Wiens et al.*, 1994]. The aftershock plane is coincident with the steeply dipping plane of the first subevent focal mechanism.

best average focal mechanism for the March 9 event. The solution (strike = 8°, dip = 76°, slip = 252°, duration = 13 s, moment = 3.05 x 10^{20} Nm) is very similar to the Harvard centroid moment tensor (CMT) solution (strike = 7°, dip = 77°, slip = 246°, moment = 3.07 x 10^{20} Nm) [*Dziewonski et al.*, 1994] obtained without the regional waveforms. However, higher-frequency waveforms show polarity reversals in the *P* waveforms from stations in North America, Antarctica, and Hawaii as well as in the *SH* waveforms from Australia due to a change in focal mechanism during the rupture. The change also causes significant amplitude effects on waveforms in other directions. Figure 2 shows focal mechanisms for the beginning and the end of the rupture, as well as the long-period focal mechanism. The focal mechanisms for the beginning and end of the rupture are clearly delineated by changes in *P* wave polarities determined from broadband displacement records. The change in focal mechanism consists largely of a 30° rotation in strike and a 15° steepening of the vertical nodal plane, with a smaller change in the horizontal plane orientation. The focal mechanism determined from the long-period inversion is approximately the average of the solutions for the beginning and the end of the rupture. The mechanism change has also been noted by *Lundgren and Giardini* [1995] and *Goes and Ritsema* [1995]. The change of mechanism will be determined more quantitatively as a function of position on the fault plane in the waveform inversion section of this study.

Well-located aftershocks from the March 9 event define a plane that is consistent with the near-vertical nodal plane of the main shock, suggesting for the first time that deep earthquake aftershocks can delineate the fault plane [*Wiens et al.*, 1994]. All of the well-located aftershocks within 90 km of the main shock during the first day after the main event lie on a near vertical plane. The least squares fit of a plane to the aftershocks has a strike of 30° and a dip of 68°, and none of the aftershocks are located more than 5 km from this plane [*Wiens et al.*, 1994]. This orientation is nearly identical to the steeply dipping nodal plane from the beginning of the rupture (strike = 25°, dip = 66°), strongly suggesting that the near-vertical plane represents the fault plane (see Figure 2). Most of the well-located aftershocks are contained in a 45 km x 30 km region that represents the intersection of the fault plane and the seismically active slab, as defined by previous seismicity. However, two aftershocks are located on the fault plane but outside the seismically active slab, one to the NE and the other to the SW of the hypocenter [*Wiens et al.*, 1994]. An analysis of all the aftershocks also suggests a NE rupture direction in that 15 of the first 17 aftershocks are located to the NE of the epicenter [D. A. Wiens et al., manuscript in preparation 1997].

Despite the clear association of the aftershocks with the near-vertical plane of the main shock focal mechanism, there has been some debate about which fault plane ruptured. *Lundgren and Giardini* [1995] found that the teleseismic body waveforms show a slight preference for the near-vertical plane. *Goes and Ritsema* [1995] concluded that they could not resolve which fault plane ruptured, and *Antolik et al.* [1994] found a slight preference for the near-horizontal fault plane from an analysis of teleseismic waveforms.

In this study, we will characterize the rupture of the Tonga event by inverting teleseismic waveforms with an expanded data set that includes both the broadband data from our local deployment and teleseismic data from IRIS and Geoscope stations, giving us good coverage of the entire focal sphere. We will investigate the ambiguity about the fault plane orientation and the rupture direction by studying both *P* and *SH* waves with a method that takes into account the change in focal mechanism. Finally, we will locate the pulses of moment release from the Tonga event relative to the background seismicity of the Tonga slab and well-located aftershocks to study the relationship between the Tonga rupture, the slab, and the aftershocks.

Directivity Analysis and the Direction of Rupture Propagation

Both the regional and teleseismic broadband waveforms show strong evidence of northeastward rupture propagation during the main shock. To examine the directivity quantitatively, we picked observed rupture durations at teleseismic and local stations. This procedure allows us to identify the location of the rupture termination point, assuming the rupture is approximately unilateral. Several of the regional stations showed complicated waveforms that probably result from complex propagation paths between the source and receiver. Therefore we applied an empirical Green's function (EGF) deconvolution technique [*Ammon et al.*, 1993] to remove the effects of upper mantle structure and isolate the relative source time functions (RSTF) for both *P* and *S* waves for the regional stations. For our empirical Green's function we used an aftershock (m_b 5.2) of the March 9th event (March 10, 12:25 UT) that had a similar focal mechanism to the main shock and was located in the middle of the fault plane defined by the aftershocks. In general, the deconvolution is stable up to 0.5 Hz at the Fiji stations and 0.33 Hz at the Tonga stations. The large change in focal mechanism during the main shock distorts the shape of the RSTFs. However, for stations which are not near a node in the radiation pattern, the duration of the time function is robust. Figure 3 shows RSTFs for regional stations along with estimates of the start and end of the rupture and the total apparent rupture duration. The time functions at AFI (located to the northeast) are short and triangular, while in the other directions the pulses are longer and more complicated showing multiple peaks. This systematic variation in both duration and shape suggests a rupture propagating to the northeast. For teleseismic stations (30°<delta<90°), ray paths bottom in the lower mantle and do not show significant effects of propagation; therefore the rupture durations were picked from displacement *P* waveforms. The displacement waveforms generally appear uncontaminated by propagation or near-receiver structure and the duration is easily picked in most cases (Figure 4).

Figure 5 shows stereonet plots of the observed rupture durations which we picked from regional *P* and *S* wave RSTFs (upper focal hemisphere) and teleseismic displacement *P* waveforms (lower focal hemisphere). For the few seismic stations at distances between 10° and 30°, the aftershocks were not large enough to use as EGFs, and the effects of upper mantle structure on the waveforms are significant. We did not use these stations, although we note that the displacement waveform at SNZO (distance is 24°, azimuth is 190°) showed a long-duration, compatible with north-northeastward rupture propagation. The end of the rupture was not clearly identifiable at most stations in China and Alaska; these stations plot near the *P* wave nodal plane at the end of the rupture, such that the decrease in body wave amplitude due to the focal mechanism change cannot be distinguished from the termination of rupture. The stations used provide good azimuthal coverage on both the lower and upper focal spheres, and the pattern of short observed durations to the

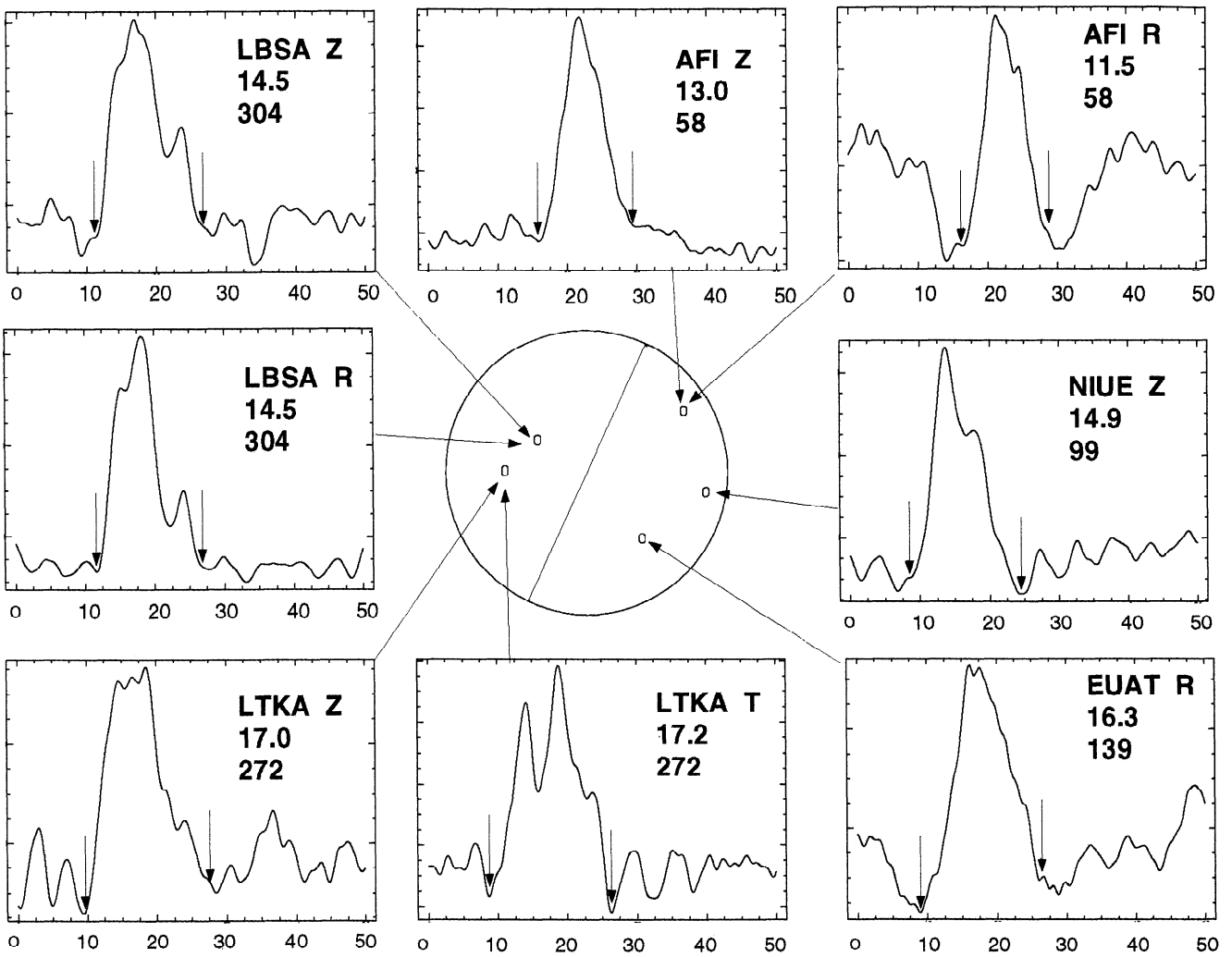

Figure 3. Relative source time functions determined from *P* and *S* waves at regional stations in the southwest Pacific using an empirical Green's function technique. The upper focal hemisphere in the middle shows the takeoff angle for each station at the source, with the line indicating the strike of the plane of aftershocks denoting the fault plane. The arrows indicate estimates for the beginning and end of the main pulse of moment release observed at each station. The scales at the bottom of the records are in seconds. Each waveform has a label indicating the station abbreviation, the component, the duration of the pulse in seconds, and the azimuth in degrees. Short triangular pulses are observed at stations to the northeast, whereas the pulses lengthen and become more complicated for stations to the southeast and the west, indicating northeastward rupture propagation.

NNE, indicative of rupture toward the NNE, is the dominant feature.

The arrival time at each station for the rupture termination event was then determined by adding the observed duration to the observed first arrival. These arrival times were then used in an inversion for the location of the end of the rupture relative to the main shock hypocenter and the aftershocks. We determined the relative positions and uncertainties of the hypocenter, the end of the rupture, and the well-located aftershocks by inverting *P* and *S* phases from the regional network along with teleseismic *P*, *pP*, and *PKP* phases using a hypocentroidal decomposition algorithm [*Jordan and Sverdrup*, 1981]. This method uses arrival times from different events at the same station to constrain earthquake relative positions within a limited source region, thus minimizing the effect of velocity heterogeneity along the ray paths. The results are displayed and analyzed using a three-dimensional graphics package that renders the 95% confidence volumes of the earthquake locations as geometric solids [*Wiens et al.*, 1993].

This procedure for locating the rupture termination is valid as long as the rupture is primarily unilateral. Synthetic tests using a bilateral horizontal rupture show that the procedure locates the rupture termination very near the epicenter, but with a large error ellipse, since the azimuthal distribution of observed rupture durations produced by a bilateral rupture does not exhibit a pattern consistent with a single termination location. This suggests that for a bilateral or circular rupture, the procedure effectively locates the centroid of the rupture termination event, but the observed durations are not well fit. In the case of the March 9 event, the pulse durations at the various stations show a pronounced azimuthal pattern which must be interpreted as a dominantly unilateral rupture, justifying the use of this procedure.

Plate 1 shows the location of the end of the rupture relative to the aftershocks and onset of rupture (hypocenter). Plate 1a is a

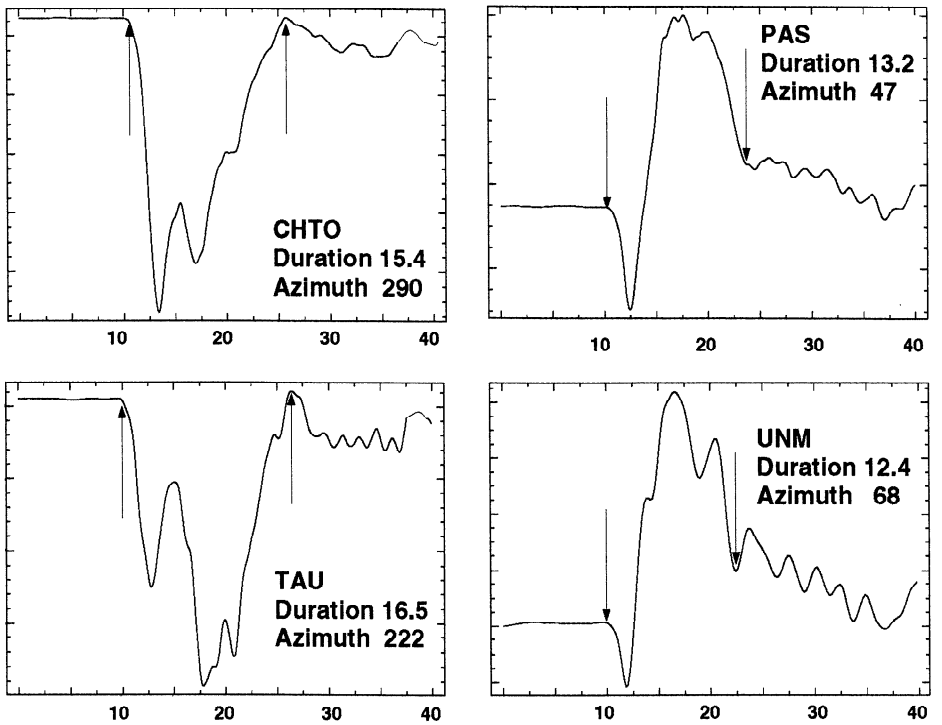

Figure 4. *P* wave displacement seismograms at four azimuthally distributed teleseismic stations with the same labeling as Figure 3. The shortest durations are found to the northeast, suggesting northeastward rupture propagation. Note the polarity reversals for North American stations (PAS and UNM) indicative of the change in focal mechanism.

view from the northeast looking along the strike of the near-vertical fault plane. The red ellipsoid denotes the location of the end of the rupture, the white ellipsoid is the hypocenter, and the green ellipsoids are the aftershocks. A small foreshock (International Seismological Centre (ISC) m_b 5.2, our estimate m_b = 4.3) occurred on March 2, 1994, and is coplanar with the aftershock plane but located 25 km shallower and to the northeast (yellow ellipsoid) [D. A. Wiens et al., manuscript in preparation, 1997]. The end of the rupture is located 39 km from the hypocenter at a direction of N20°E, along the strike of the aftershock plane at approximately the same depth as the hypocenter. The 2 standard deviation error ellipse for the end of the rupture is approximately the same size as the error ellipses for aftershocks with similar station coverage. This suggests that the end of the rupture is a coherent feature resulting from a predominately unilateral rupture.

Plate 1b is a view from the northwest, perpendicular to fault strike. The aftershock distribution shown in Plate 1b indicates a relatively symmetrical distribution about the hypocenter, without a clear directional preference for rupture propagation. The large

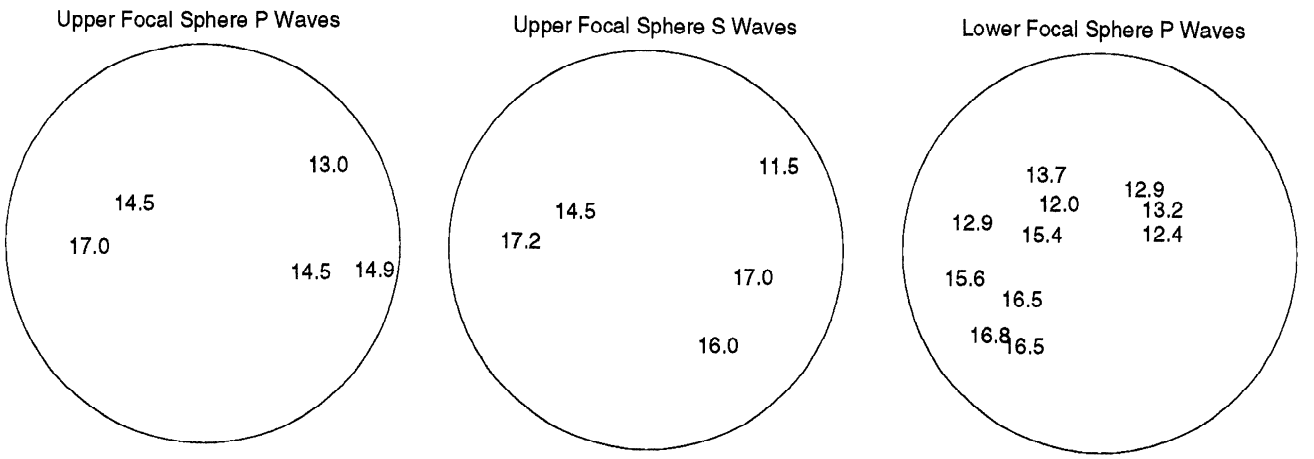

Figure 5. Stereonet plots of observed rupture durations from relative source time functions of local *P* (left) and *S* (middle) and teleseismic *P* wave (right) displacement records. The duration in seconds is plotted at the point corresponding to the appropriate take off angle and azimuth. The primary feature of both regional and teleseismic records is the short observed rupture durations at stations to the northeast.

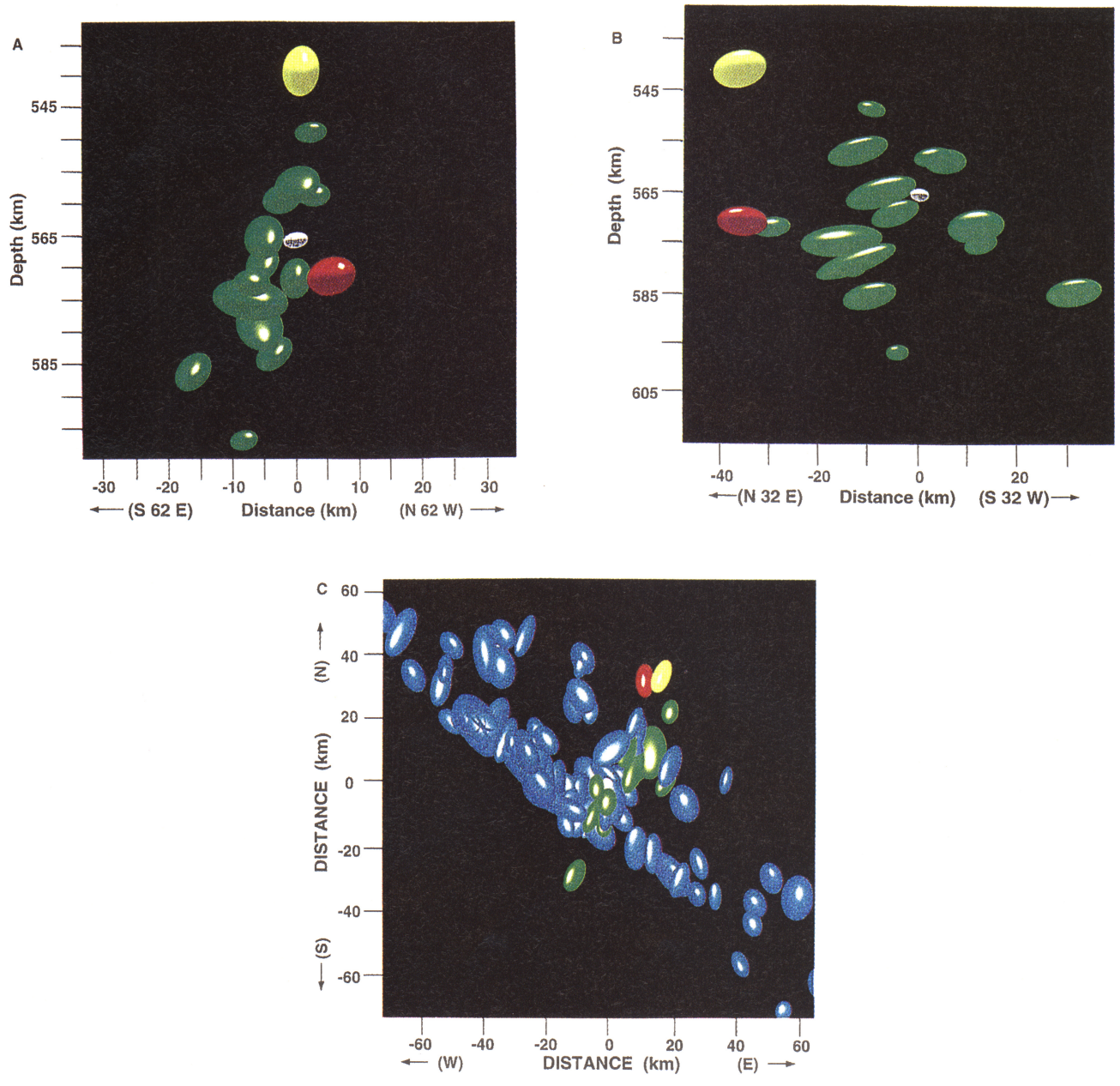

Plate 1. Three-dimensional views of the best located aftershocks, the main shock hypocenter, and the rupture termination point as determined by a hypocentroidal decomposition inversion [*Jordan and Sverdrup*, 1981]. Each panel shows the 95% confidence ellipsoid for each aftershock (green ellipsoids), as well as the main shock hypocenter (white ellipsoid), a small foreshock that occurred 1 week prior to the main shock (yellow ellipsoid), and the end of the rupture (red ellipsoid). All arrival times and associated uncertainties were picked by our research group except that teleseismic arrival times compiled by the monthly PDE bulletin were added. Only aftershocks showing 95% confidence semiaxis lengths of <9 km are plotted. All of the aftershocks have at least seven arrival times from both our regional network and teleseismic stations. (a) A view from N30°E, edge-on to the plane of the aftershocks, showing that the end of the rupture and the foreshock are located on the same northeast striking plane as the aftershocks. (b) A view from N60°W, perpendicular to the view in (a). This figure shows that the aftershock zone is roughly circular with a radius of about 30 km, and that the end of the rupture lies slightly farther to the northeast than the furthest aftershock in the NE direction. (c) A map view of seismicity from 530 to 590 km depth in the region of the March 9 event. Background seismicity (blue ellipsoids) with arrival time data taken from the 1980-1987 (ISC) and 1990-1995 (PDE), were inverted along with the aftershocks (green), the foreshock (yellow), the hypocenter (white), and the rupture termination point (red). One hundred and fifty earthquakes with uncertainty semiaxis lengths less than 9 km and at least 2 upgoing arrivals (local P or teleseismic pP phases) were used to delineate the active slab. The slab in the area of the March 9 main shock is nearly vertical. The aftershock plane crosscuts the seismically active slab and extends into the surrounding aseismic region. The foreshock and the other adjacent earthquake are located above the end of the rupture (red ellipsoid), which is located about 15 km into the previously aseismic region.

directivity signal in the waveforms indicates that the moment release propagated dominantly to the northeast and suggests that the moment release probably does not extend to all the aftershocks, as will be discussed in more detail in the waveform inversion section of this paper. Because the rupture termination point is at almost the same depth as the hypocenter and located along the strike of the vertical fault plane, it is consistent with both the near-vertical and near-horizontal fault planes. However, the directivity study requires that the rupture propagated primarily to the northeast at an azimuth which coincides with the strike of the plane determined from the aftershock locations and the first motion focal mechanism, providing strong evidence that the event occurred along the near-vertical fault plane (Plate 1a).

To examine the relationship between the various features of the March 9 rupture and the active deep seismic zone, we performed a relative location of the aftershocks, the hypocenter, the rupture termination point, and background seismicity. The background seismicity data includes 150 earthquakes from the ISC catalog between 1980 and 1987 and the Preliminary Determination of Epicenters (PDE) from 1993 and 1995, including arrival times read from our temporary broadband network between 1993-1995. The Tonga slab is nearly vertical in the region of the March 9 event and strikes N50°W, as can be seen from the map view of our relocation in Plate 1c. There are two parallel planes of background seismicity which form a indistinct double seismic zone when viewed in cross section. The seismic zone is about 35 km thick, with the thickness increasing to 40-45 km above the main shock, in the vicinity of the foreshock. The near-vertical plane defined by the aftershocks is almost perpendicular to the strike of the slab, and the aftershock zone crosscuts the seismically active slab. There are two well-located aftershocks in the first 18 days after the main shock which are located outside the main zone of seismicity [*Wiens et al,* 1994]. The end of the rupture is located about 15 km beyond the background seismicity to the northeast, about 30 km beneath the small foreshock and another 1994 earthquake near the foreshock, and a few kilometers farther into the aseismic region than the outlying aftershock.

Waveform Inversion for Moment Distribution and Focal Mechanism Change

Method

To model the waveforms of the March 9 event, we utilized a method which is similar to that of *Mori and Hartzell* [1990] and *Dreger*[1994]. This method solves for the spatial distribution of moment release, assuming a particular fault orientation and a constant rupture velocity and rise time. We have modified this method so that we could combine both regional and teleseismic data in our inversion, and so we could solve for the focal mechanism change which has a pronounced effect on the waveforms via the change in radiation pattern.

The fault plane is parameterized as a grid of nodes, each representing a square subfault. To limit the number of model parameters and still be able to solve for the change in focal mechanism, the nodes are grouped into regions of constant focal mechanism, and the focal mechanisms of the regions are solved for. We used a node spacing of 3 km and 12 regions of constant focal mechanism, each of which have dimensions of 10-15 km. The synthetic displacement seismogram at the jth station is given by

$$SD_j(t) = \sum_{i=1}^{n} G_{ij}(t) m_i \quad (1)$$

Where n is the number of nodes, G_{ij} is a theoretical Green's function relating the slip at the ith node to the waveform observed at the jth station, and m_i is a scaling factor proportional to the moment release of the ith subfault.

The Green's functions (G_{ij}) are computed using geometric ray theory. The radiation pattern term, the free surface term, and the geometrical spreading term are taken from *Kanamori and Stewart* [1976]. Average seismic attenuation or Q was calculated for teleseismic stations using the PREM model, and for local stations, the Q values were taken from the study of *Roth et al* [1994]. Because the phases being modeled either bottom in the relatively homogeneous lower mantle or travel along steep upward paths from the source, propagation effects are minimal and geometric ray theory provides a good approximation. We tested the geometric ray theory synthetics against reflectivity synthetics calculated for standard Earth models and found the differences to be minimal. A few regional stations showed complicated propagation effects due to the structure of the slab, as identified by complicated arrivals for aftershocks. These stations were not used in the inversion.

We computed the Green's Functions for each node-station pair by convolving the ray theory synthetic with a source time function appropriate for an individual node and applying a delay (λ_{ij}) which is a function of the position of the node on the fault plane. The delay time (λ_{ij}) of a particular node-station configuration is given by

$$(\lambda_{ij}) = T_j + (d_i/v) + \Delta t_{ij} \quad (2)$$

where T_j is the travel time from the hypocenter to the jth station which was picked from the displacement records, d_i is the distance from the hypocenter to the ith node, v is the rupture velocity which is assumed to be constant in all directions and is determined using a grid search, and Δt_{ij} is the change in the travel time due to the node being at a different absolute position in space than the hypocenter [*Flinn*, 1965]. Because T_j is the observed travel time from the epicenter to the stations, the nodes are located relative to the epicenter, not in absolute space. This distinction will allow us to map the regions of high moment release from the waveform inversion solution onto the locations of the aftershocks and the rupture termination point from the previous section.

We use this method to model P and SH wave displacement seismograms obtained by deconvolving the instrument response from the original broadband seismograms. Both the data and the synthetic are low pass filtered at 0.4 Hz to remove high-frequency effects that are usually due to local site effects. A trapezoidal source time function is assumed for each subfault. This time function is presumably the convolution of the rise time (duration of faulting at a given point) with the propagation time between nodes. In practice, different values for the time function duration were tested, and the one providing the minimum misfit was chosen. There was not a significant difference in misfit for a reasonable range of values; the final results were generated with a time function duration of 2.5 s for each node.

Substituting the observed data for the synthetic seismogram in (1), we obtain a matrix equation which can be inverted:

$$\begin{bmatrix} G \\ \Theta S \end{bmatrix} m = \begin{bmatrix} D \\ 0 \end{bmatrix} \quad (3)$$

where G is the matrix of Green's Functions, m is a vector of the m_i values in (1), and D is a vector of the displacement seismograms. We added a constraint to (1) that minimizes the second derivative of the spatial distribution of the moment release in the solution [*Menke*, 1989; *Ammon and Vidale*, 1993]. S is the second spatial derivative matrix, and Θ is a scalar which controls the strength of the smoothing constraint [*Dreger*, 1994]. We also scale the rows of both the G matrix and the D matrix so that stations with large amplitudes do not dominate the inversion. We then perform a standard nonnegative least squares inversion [*Lawson and Hanson*, 1974] for the m vector.

Synthetic seismograms are then calculated from the moment distribution using (1). We scale the maximum of each synthetic to the maximum of the corresponding data record. We use a scaling factor specific to each station rather than a constant scaling factor because an amplitude error at one station can disrupt the effectiveness of the focal mechanism grid search. In practice, even though we are modeling both local and teleseismic records, the difference between the scaling factors for most stations is only ±10-20% from the median scaling factor. The misfit is calculated as the sum over all records of the squared differences between data and synthetics, normalized by the sum of the squared data.

Because a relative scaling procedure is used in determining the moment distribution, we assume that the sum of the moments of all the nodes is equal to the long-period moment of the event, as determined by long-period waveform inversion. The slip on each subfault is then given by

$$Slip_i = \frac{M_o\, m_i}{A_i\, \mu\, m_t} \tag{4}$$

where m_t is the sum of all the m_i values, A_i is the area of each subfault, and μ is the rigidity at the source.

A grid search is performed to determine the values of the ancillary variables included in the inversion (rupture velocity, time function duration of each node, and focal mechanism of each region of nodes). Determination of the focal mechanism as a function of position on the fault was the most tedious part of this operation. The body waveforms proved to be quite sensitive to the exact parameterization of the fault plane in terms of the faulting regions. For the final inversions, the number of regions was increased and the boundaries between regions were adjusted to delineate the exact locations in which the focal mechanism changed.

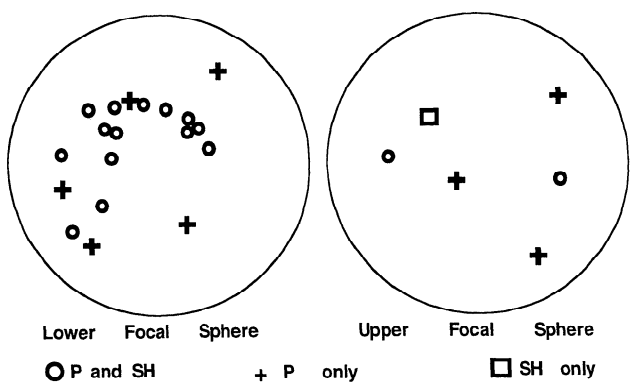

Figure 6. Stereonet plots of the station coverage on the (left) lower and (right) upper focal hemispheres for the waveform inversion of the main shock. Symbols, which are plotted at the azimuth and takeoff angle of each station, denote which phases from that station were used in the inversion. The combination of teleseismic and local data provides good coverage of both the upgoing and downgoing focal spheres. The station name, distance, and azimuth are tabulated in Table 1.

Table 1. Station Set Used for Waveform Inversion

Station	Distance, deg	Azimuth deg	Station	Distance, deg	Azimuth, deg
PAS	77	47	NWAO	59	242
MAJO	68	323	PMSA	84	157
GUMO	48	308	TUC	81	52
XAN	86	307	PET	74	346
TAU	38	222	LKBA	1	246
CTAO	33	261	COR	80	36
AFI	7	58	CHTO	89	290
LBSA	3	308	ANMO	86	51
LTKA	4	273	TATO	73	304
EUAT	5	137	BJI	84	315
VAVA	4	99	CAN	34	233
PMG	34	280	KIP	44	28
COL	86	12	INU	68	322
YSS	74	333	UNM	86	68

Resolution Tests

We have performed a number of resolution tests to determine how well the station configuration used for the inversion of the March 9 data (Figure 6 and Table 1) can resolve features of the moment release distribution and the focal mechanism change. We start with an assumed moment distribution and fault plane (strike = 30° and dip = 70° for all cases shown here) and then calculate synthetic data with (1) for all of the stations and phases. Noise was added to the "data," which were then low pass filtered at 0.4 Hz. In the following sections, we present three tests designed to test the ability to resolve smoothly varying features in the moment release distribution, sharply varying features in the moment distribution, and the change in the focal mechanism during the rupture.

Test 1, smoothly varying moment distribution. The moment distribution assumed for this test is shown in Figure 7a. It consists of three roughly circular subevents with diameters of about 10 km, located at different points on the fault plane. For this test, a constant focal mechanism was assumed for the entire rupture. The magnitude of the moment release of the subevents decreased slowly in the radial direction from the center of each subevent resulting in a smooth moment distribution. The maximum magnitude of the moment distribution varied between the subevents. Figure 7b shows the moment distribution obtained from the inversion. Because the subevent located farthest to the right was the subevent closest to the hypocenter, it is the most well resolved of the three. The two subevents farther from the epicenter are less well resolved, with the moment release spread over a larger region in the inversion result. This lack of resolution for later subevents results from the existence of more nodes with the same time delay from the hypocenter (distance from epicenter divided by rupture velocity). The smearing of the moment release due to this effect occurs along an arc of constant radius from the hypocenter. The radial extent of the first subevent is also slightly exaggerated due to the limited frequency

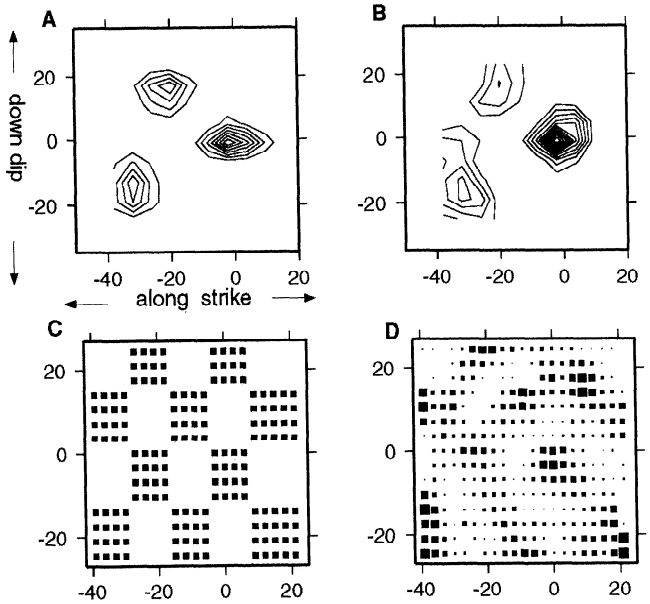

Figure 7. (a) A contour plot of the moment release distribution used in generating the data for the first resolution test. The scales are in km, and the hypocenter is located at (0, 0). In the first test the fault plane was assumed to have constant focal mechanism. (b) The moment release distribution produced by inversion of the synthetic data for test 1. The main features of the initial model are preserved, including the total moment release of each of the subevents, but the later subevents have been smoothed. (c) The moment distribution assumed for the third test. All nodes were assigned either a value of 1 or 0 forming a checkerboard pattern. (d) Result produced by the inversion of data generated by this pattern. Light and dark patches are visible corresponding to the checkerboard pattern, but overall, the data set is not capable of resolving the sharper details of a complex pattern.

band of the inversion and the smoothness constraint placed on the inversion. Despite the smearing, the location of the three local maxima is well reproduced in the inversion result. The absolute maximum amplitudes of the second and third subevents are reduced relative to the first event because the moment release is spread out over a larger area. However, the total moment of the respective subevents is recovered to within 4%.

Test 2, focal mechanism change. Using the same moment distribution as in test 1 (shown in Figure 7a), we produced and inverted synthetic data using different focal mechanisms for the three subevents. In all cases, the inversion determined the correct focal mechanism for each event, and the resolution for the spatial distribution of the moment release was similar to that shown in Figure 7b. The resolution for the focal mechanism parameters depended on how the stations were distributed with respect to the *P* and *SH* nodal planes of the different mechanisms, with good resolution obtained in cases where the focal mechanism change produced polarity reversals at a number of stations. This is encouraging for the study of the March 9 event because there are a large number of both *P* and *SH* waveforms which show polarity reversals.

Test 3, sharply varying features. We produced synthetics for a checker board pattern of moment release shown in Figure 7c. All nodes in the synthetic data had either a uniform slip or no slip as shown in Figure 7c, with the dimensions of the regions of the order of 10-15 km. The slip distribution obtained from the inversion is shown in Figure 7d. While the rectangles of high and low slip are visible in the inversion result, the boundaries between the areas of slip and no slip are not sharp, and small amounts of slip are found even in the center of some of the no-slip regions. This test shows that the inversion can recover the general spatial pattern of moment release but cannot resolve discrete boundaries which occur in the checkerboard pattern when the patches of moment release are on the scale of 10-15 km.

These resolution tests show that the locations of the major pulses of moment release and the total moment release of the subevents should be resolvable with our station set. Furthermore, any change of focal mechanism should be well resolved. However, we may expect limited resolution of sharp features and smearing of the spatial distribution of the moment release, particularly farther from the epicenter. Other resolution test we have conducted show that the inclusion of the local stations (with upgoing ray paths) is essential for obtaining the generally good resolution obtained in this study.

Analysis

Inversion of the March 9, 1994, Tonga Event

The inversion was applied to a data set consisting of 22 teleseismic and 5 regional *P* waveforms and 17 teleseismic and 3 regional *SH* waveforms which provided excellent station

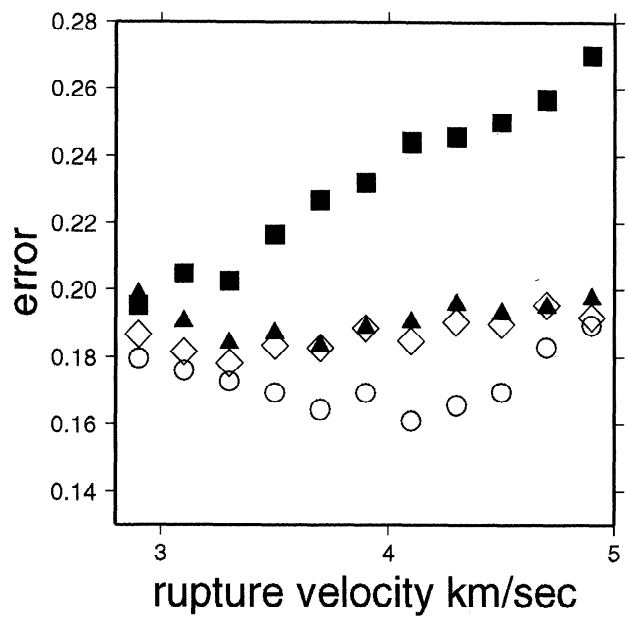

Figure 8. Plot of error as a function of rupture velocity for four different waveform inversion solutions. The moment release was assumed to be limited to either the near-vertical plane or the near-horizontal plane. Open circles show error values for moment release along the near-vertical nodal plane, and open diamonds show results for the near-horizontal plane. In addition, results were calculated where the moment release was constrained to a 40 km wide previously active seismic zone along the vertical plane (solid squares) and the horizontal plane (solid triangles). The unconstrained solution for the near-vertical nodal plane provides the best solution and indicates a rupture velocity of about 4.1 km/s. Solutions where the moment release is confined to the seismically active slab core show higher error values, indicating that the rupture propagated into previously aseismic regions surrounding the active seismic zone.

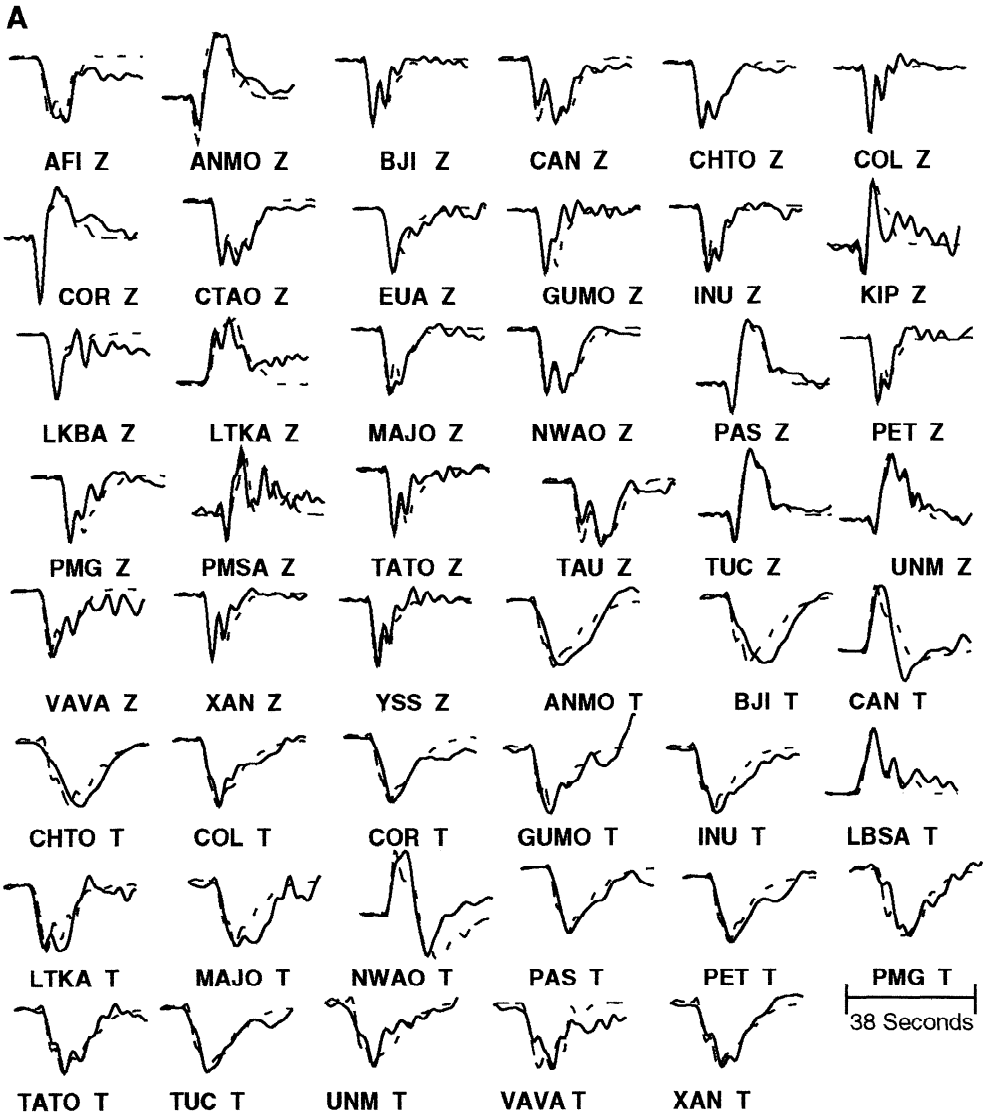

Figure 9. Waveform fits from the inversion of the March 9 displacement waveforms for the unconstrained (a) near-vertical and (b) near-horizontal fault planes. Data are shown by the solid line and synthetics are shown by the dashed line. Z denotes a vertical component *P* wave and T denotes a transverse component *S* wave. The records are 38 s long. The waveform fits of the two models are relatively indistinguishable except for a few records such as the station PMSA *P* waveform, which is better fit by the near-vertical fault plane.

coverage (Figure 6 and Table 1). Waveforms were selected based on their signal to noise ratio and to maximize the coverage of the focal sphere for both *P* and *SH* waveforms. Regional waveforms from the PASSCAL station on Niue were omitted from the inversion because records of larger aftershocks showed extremely complicated waveforms due to propagation effects along the path up the slab. We also did not use the radial *S* wave components because of greater contamination from local converted phases and the receiver structure.

The waveforms were inverted assuming that the moment release was confined to either the near-vertical or the near-horizontal nodal planes. The first motion fault plane (strike = 25°, dip = 65°) rather than the fault plane from the long-period solution was chosen to represent the near-vertical plane since the aftershocks align along the first motion fault plane [*Wiens et al,* 1994]. Inversions were also run in which the moment release was constrained to occur inside the seismically active zone, as defined by previous slab seismicity (see Plate 1c). Figure 8 plots the misfit of the solutions as a function of rupture velocity, assuming either the vertical or horizontal fault plane and with the rupture extent either unconstrained or constrained to lie within the active seismic zone. The unconstrained solutions show lower errors than the solutions where the moment release is confined to the active slab, especially for the vertical plane. The unconstrained vertical fault plane consistently shows a slightly lower error than the unconstrained horizontal fault plane.

The slip distributions for the best vertical fault and horizontal fault solutions are shown in Plates 2a and 2b, respectively, and the waveform fits for these solutions are shown in Figures 9a and 9b. Both models fit the data well, and the differences between them are small. From the resolution test described above we know that low amplitude features in Plates 2a and 2b may be

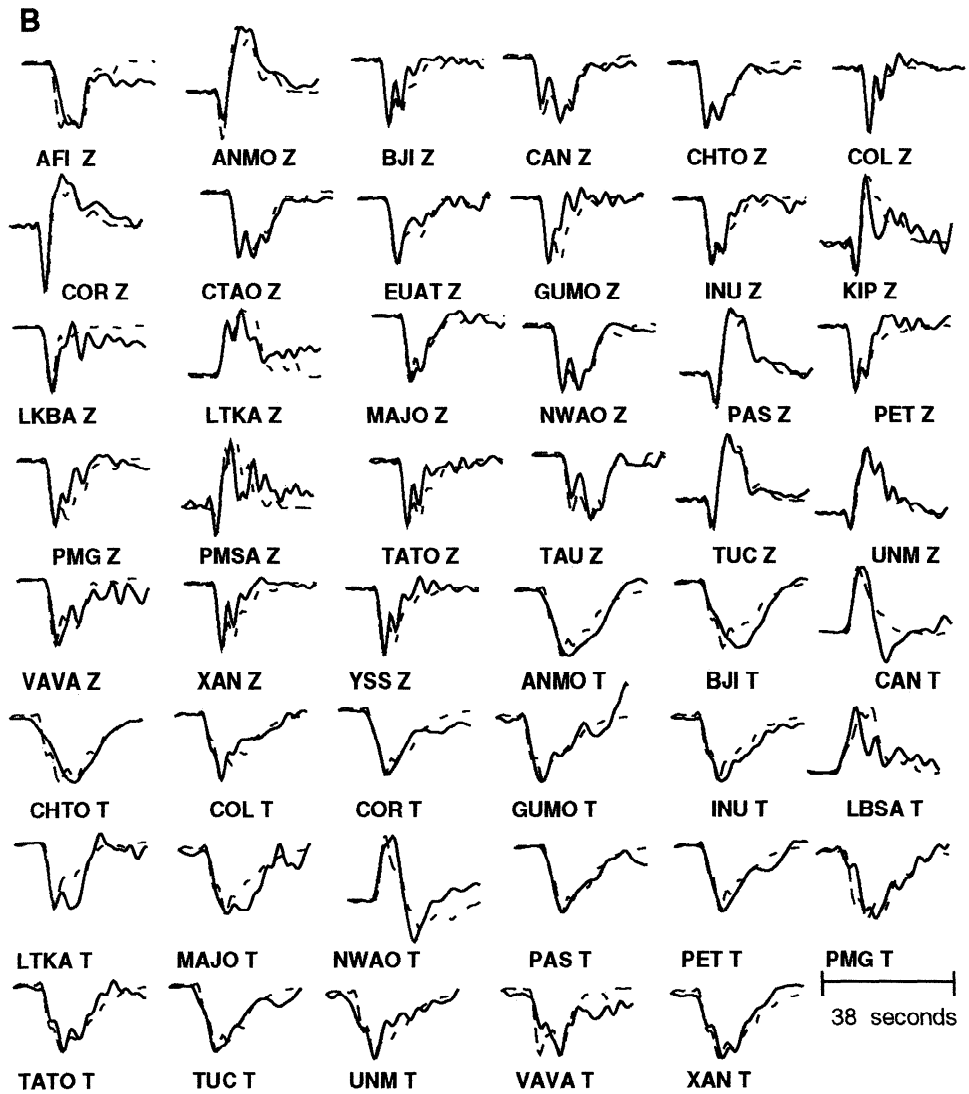

Figure 9. (continued)

artifacts. The high amplitude features such as the zone of slip which extends to the NE and shallower in Plate 2a should be well resolved if the correct fault plane is chosen. Differences in error on the order of 0.005 are subtle but are visible in the waveform fits at key azimuths. Only small differences in the waveform fit exists for rupture velocities between 3.7 and 4.3 km/s for the vertical plane and similarly for velocities between 3.3 and 4.1 km/s for the horizontal fault plane. The difference in error of about 0.02 between the best fit for the unconstrained vertical and horizontal planes provides a slightly better fit to most waveforms and clearly visible improvements to waveforms at critical azimuths such as PMSA .

The best model for the slip distribution is shown in Plate 2a. The rupture occurred on the near-vertical fault plane of the first motion focal mechanism, with a strike of approximately 25° and a dip of 70°. A large focal mechanism change occurred in two stages during the rupture, and the resulting change in radiation pattern caused the polarity reversals and other waveform features at many of the stations. The rupture propagated dominantly to the northeast and slightly shallower, with three main regions of moment release. The rupture terminated close to the location of the outlying aftershock nearly 40 km to the NE of the hypocenter. The location of the rupture termination point is also immediately below the location of the small March 2 foreshock. In the following sections, we discuss the major features of this model.

Fault Plane Choice

We find that the near-vertical nodal plane provides a slightly better fit to the waveforms than the near-horizontal nodal plane. The fit of the two models to the waveforms is not grossly different (compare Figures 9a and 9b), although the superior fit of the near-vertical plane is evident in several of the waveforms. In the absence of any additional information, it would be difficult to argue that the waveforms demonstrate conclusively that the faulting occurred along the vertical plane, particularly in view of the relatively small error difference and the assumptions made by the inversion, such as constant rupture velocity and constant rise time for all the nodes. However, the agreement between the aftershock locations, showing that the aftershocks align along the near-vertical fault plane and that the initial aftershocks are located to the NNE of the epicenter, the directivity analysis, showing that the rupture propagated to the NNE along the strike of the vertical fault plane, and the waveform inversion results provide compelling evidence in favor of the steeply dipping fault plane.

The lack of resolution for the fault orientation in the waveform

inversion results primarily because the rupture propagation direction, toward the NNE, is close to the null axis of the focal mechanism and the vertical dimension of the rupture is rather limited. The rupture comes close to approximating a line source propagating horizontally toward the NNE. Thus, when the moment release is required by the inversion to be localized along the near-horizontal plane, an adequate fit is also obtained. Our best fitting solution for the horizontal fault plane (Plate 2b) shows a dominantly northward rupture, with other regions of moment release to the ENE and ESE of the hypocenter. This distribution of moment release is capable of generating waveforms which are very similar to a nearly unilateral NE rupture propagation on a vertical fault plane.

The lack of resolution also results because the spatial distribution of moment release has a second-order effect on the waveforms relative to the change in focal mechanism and the time distribution of moment release (source time function). The spatial distribution produces at most a difference of up to 5 s in the duration of the *P* waveforms, whereas the focal mechanism change produces changes in waveform polarity at a number of stations and significant changes in the relative amplitude of the major pulses at all the stations. Thus distinguishing between two fault plane solutions which generally permit similar northward ruptures is more difficult than resolving the change in focal mechanism or the source time function. This is illustrated by the fact that we obtain virtually identical focal mechanism changes and source time functions, regardless of which nodal plane is assumed to represent the fault plane. The focal mechanism change in both models consists of a change with time from (strike 25°, dip 66°, slip 240°) to (strike 355°, dip 85°, slip 235°). Similarly, the source time functions obtained for the two models are very similar, showing two to three main pulses of moment release with a total duration of about 14 s (Figure 10).

Previous studies of the March 9 event based solely on teleseismic waveforms have reached varying conclusions about which nodal plane represents the fault plane. *Lundgren and Giardini* [1995] studied the event using the method of *Kikuchi and Fukao* [1985] which determines the location and focal mechanism for a series of subevents. They found that the near-vertical plane gave a somewhat better fit and that the distribution of subevents for the vertical plane gave a simple linear rupture propagation while the horizontal plane gave a more chaotic distribution. Their best solution, for the vertical plane, is composed of a rupture propagating along strike to the NNE at a velocity of about 3 km/s. *Goes and Ritsema* [1995] studied the event using a variety of methods, including the waveform inversion method of *Kikuchi and Kanamori* [1991]. They did not find strong evidence for rupture along either nodal plane but found evidence for vertical directivity from stacks of *pP* phases recorded in North America, which were of short duration in relation to direct *P* waveforms. On the basis of this observation, they concluded that the observed vertical directivity indicated that the rupture occurred along the near-vertical fault plane. Although no *pP* waveforms were used in generating it, the model presented in figure 10a is compatible with the *pP-P* directivity observed by *Goes and Ritsema* [1995]. Since the NNE rupture propagated updip, *pP* phases in North America would be of shorter duration relative to direct *P* phases. The degree of updip rupture propagation, 10-15 km, is similar to that proposed by Goes and Ritsema.

In contrast, *Antolik et al.* [1994] have proposed that rupture occurred along the near-horizontal fault plane, based on inversion of 19 teleseismic RSTFs. Their preferred model is somewhat similar to our model for the horizontal plane (Plate 2b), but does not include the change of focal mechanism. Their choice of fault plane was based on a slightly better waveform fit obtained with the horizontal plane, relative to their best fitting vertical plane model, which also resembles our vertical plane model (Plate 2a). We think that the reason for the different conclusions reached by our study and that of Antolik et al. is that their method does not include the change in focal mechanism, which produces a first-order effect on the waveforms due to the change in radiation pattern. They attempt to compensate for this by omitting stations that show obvious polarity reversals due to the mechanism change. There are two problems with this; first, stations in key quadrants have to be omitted due to the polarity change (for example, stations in North America which show very short durations due to the NE rupture propagation). Second, some stations included in their inversion, although not showing polarity reversals, nonetheless show significant effects of the focal mechanism change. Since the focal mechanism change is not a

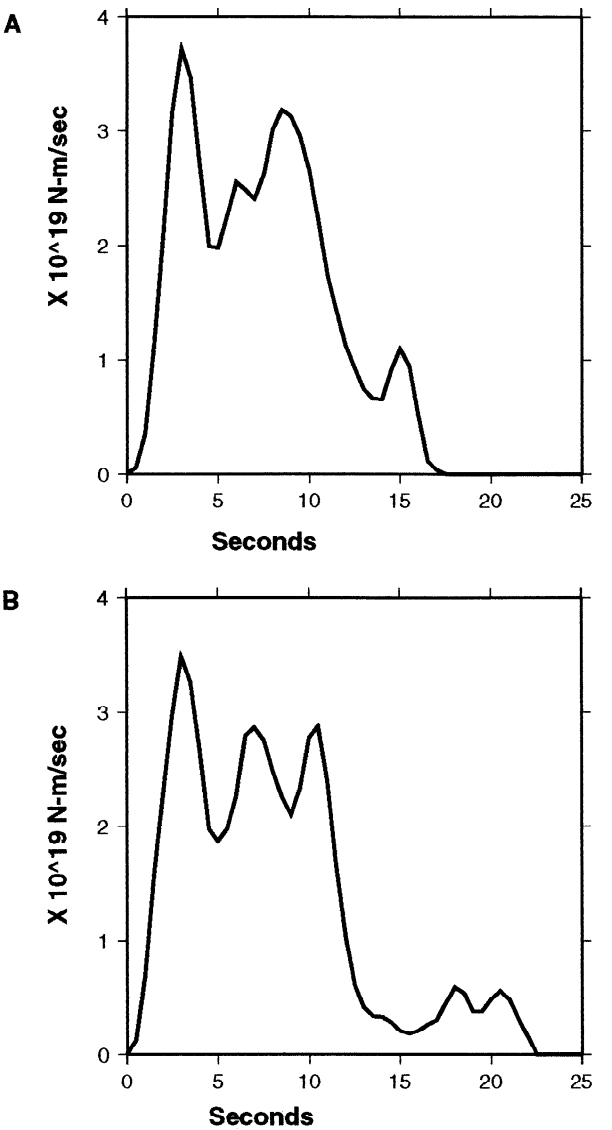

Figure 10. Plots of source time functions determined by the unconstrained inversion for the (a) near vertical and (b) near horizontal planes. The two planes produce extremely similar source time functions. The lower-amplitude features around 15-20 s probably are attempts to fit noise (coda) on the waveforms which follow the main pulse of moment release.

parameter in their model, these waveform effects generally bias their result. Finally, the Antolik et al. study did not have access to the broadband data from the regional stations of the Southwest Pacific Seismic Experiment, and thus their inversion contained no phases traveling upward from the source region.

We suggest that the best evidence for the choice of a fault plane comes from an integration of the aftershock, directivity, and waveform data, which together provide a very strong case for the near-vertical nodal plane. The aftershock locations align along the near-vertical plane; a least squares fit to the well-located aftershocks which occurred within the first day after the main shock defines a plane which deviates from the first motion nodal plane by only 5° [*Wiens et al,* 1994]. Additional recent work including smaller aftershocks shows that 16 out of 18 aftershocks in the first 2.5 hours after the main shock locate to the NNE of the epicenter [D.A.*Wiens et al.,* manuscript in preparation 1997], suggesting the early aftershocks locate near the regions of high moment release defined in this study. To propose that faulting actually occurred along the horizontal plane, one must explain not only the near-perfect alignment of the aftershocks with the auxiliary plane but also the near-absence of aftershocks along the presumed fault plane. In addition, the directivity information also provides evidence for the vertical fault plane. A least squares solution for the rupture termination point (with no constraints that it lie on either of the fault planes) suggests that the rupture termination occurred along the vertical nodal plane defined by the aftershocks, although this location is also not far off of the horizontal plane. Finally, the waveform inversion suggests that the vertical plane provides a somewhat better fit to the waveform data.

Extent of the Slip Distribution

To determine whether the moment release outside the previously active seismic zone is required by the data, we performed several inversions with slip constrained to be within the background seismicity (Figure 8). We have run the inversion with slip constrained to occur within the background seismicity zone, using a very generous estimate of 40 km for the thickness of that zone (see Plate 3). The solutions requiring that the slip be localized within the active zone had higher error than the unconstrained solutions for both possible fault planes. The constrained inversions were run with the same node spacing (3 km) as the unconstrained inversions, and the regions of constant focal mechanism were adjusted for the constrained inversions so that the change in radiation pattern with time during the rupture could be fit. The extremely large errors for the vertical plane at high rupture velocities appear to be caused by the need of the constrained inversion for a large vertical extent to fit the source time function.

The unconstrained inversion may be expected to give a better fit, due to the larger number of model parameters, so we investigate whether this improvement in fit represents a truly better solution. Source time functions and selected waveform fits for the constrained inversions are shown in Figure 11. The

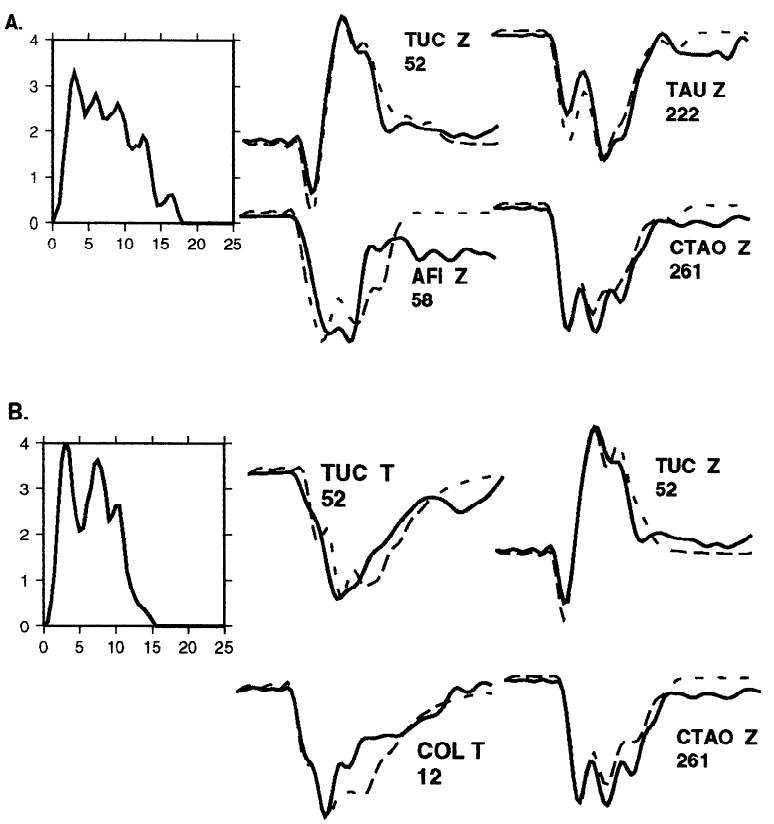

Figure 11. Source time functions and selected waveform fits for the inversions in which slip was constrained to occur within the background seismicity zone on either the (a) near-vertical or (b) horizontal nodal planes. The record durations, labels, and moment rate scales are the same as Figures 9 and 10. The constrained inversions show a higher error because the waveform features caused by the northeast rupture propagation cannot be adequately fit, as illustrated by synthetics which are too short at stations to the southwest (TAU, CTAO) and too long at stations to the northeast (TUC, COL, AFI).

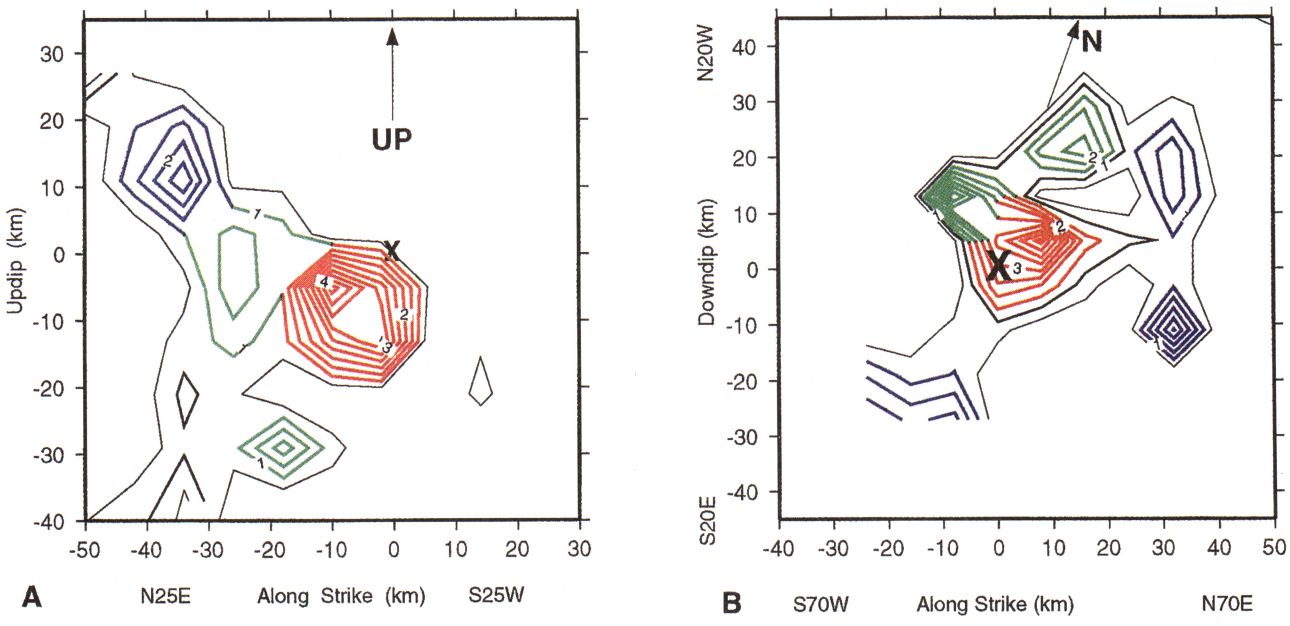

Plate 2. Contour plots of the slip distribution from the waveform inversion assuming the moment release occurs along the (a) vertical or (b) horizontal fault planes. Both Plates 2a and 2b have a contour interval of 0.5 m, and the scales are in km relative to the hypocenter (denoted by the cross). The 1, 2, 3, and 4 m contours are labeled. Contours are color coded to indicate the best fitting focal mechanism for that region of moment release. A focal mechanism of strike 25, dip 65, slip 240 is denoted by red; strike 5, dip 80, slip 235, is denoted by green, and strike 355, dip 80, slip 235 is denoted by blue. The resolution tests suggest that low-amplitude and sharply varying features are not well resolved, and some smearing of features along lines of constant radius from the hypocenter may be expected. Because this method does not assume a rupture termination time, the inversion attempts to fit any noise present in the seismograms after the end of the main pulse of moment release, resulting in low-amplitude features around the edges of the grid.

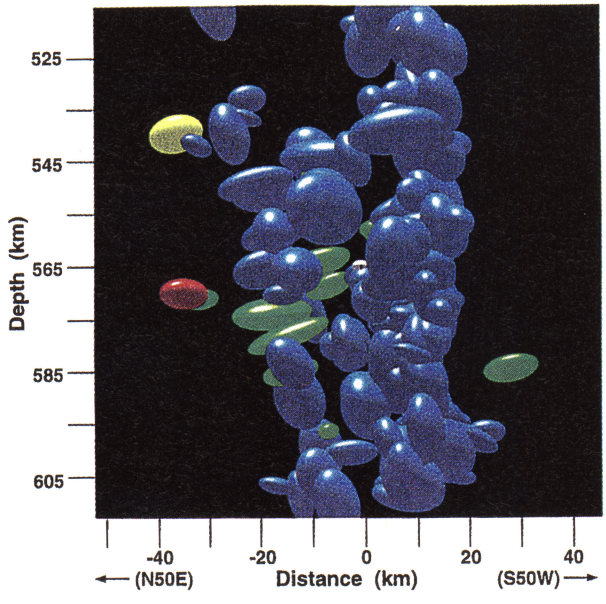

Plate 3. A cross-sectional view along the strike of the slab (N50°W) from the northwest of the area shown in Plate 1c. Blue ellipsoids denote background seismicity, the white ellipsoid denotes the hypocenter of the March 9 event, green ellipsoids denote aftershocks, the yellow ellipsoid denotes the March 2 foreshock, and the red ellipsoid denotes the rupture termination point as determined from directivity analysis. The background seismicity in this region forms an indistinct double seismic zone, and the rupture termination point is located in a previously aseismic region. At least two aftershocks also initiated in the previously aseismic region. This figure can be compared with Figure 12 to show the relationship between the mainshock moment release, the background seismicity, and the aftershock zone.

constrained inversions produce the appropriate duration source time function even though the fit is significantly poorer. The poor fit results from the inability of the constrained inversion to produce the directivity signal resulting from a rupture to the northeast. In the horizontal plane case, rupture is forced updip to the southeast, creating pulses that are too long at stations located to the northeast (TUC in Figure 11b), and pulses that are slightly too short at stations to the southwest (CTAO in Figure 11b). Similarly, for the vertical plane, constraining the rupture creates pulses that are too long in the NE direction (AFI and TUC in figure 11a) and pulses which are too short at stations to the SW (CTAO and TAU in figure 11a). The variation of observed rupture duration with azimuth cannot be fit by a rupture constrained to occur within even our conservative estimate of a 40 km thickness for the background seismicity zone.

Focal Mechanism Change

The change in focal mechanism that occurred during the March 9 rupture appears to be related to the rupture propagating beyond the normally seismogenic zone. The initial pulse of moment release has a diameter of about 20 km (Figure 12). This feature is tightly constrained by the polarity reversals at North American and Antarctic stations. Figure 12 also shows that the second and third subevents occurred in the previously aseismic region outside the active seismic zone. The outlying aftershock to the northeast (March 27) shows a focal mechanism (strike 10°, dip 70°, slip 240°) [*Wiens et al.,* 1994] that is nearly identical to the focal mechanism found by our waveform inversion for this area, providing additional confirmation for the location of the change in focal mechanism in our result. The focal mechanism change appears to have begun precisely as the rupture propagated into the normally aseismic material surrounding the active seismic zone.

The change in focal mechanism suggests a rotation of the fault strike by 30° and a 20° steepening in the fault dip. We investigated whether the spatial curvature of the fault plane produced a significant effect on the inversion results by incorporating the fault curvature into the inversion procedure described above, such that the moment release was required to occur along a curved surface which matched the change in focal mechanism as the rupture propagated northeastward. The results from this inversion were virtually identical to the results of the planar inversions described above. This is not surprising, since the maximum difference in node positions for the two fault configurations is only 5-10 km. The dominant waveform effect of the change in focal mechanism is produced by the changing radiation pattern, not by the actual curvature in space of the fault.

The results of this inversion also explain why the plane defined by the aftershocks shows better agreement with the focal mechanism of the first subevent than with the average or long-period focal mechanism [*Wiens et al.,* 1994]. Only one of the 15 well-located aftershocks is located in the region of the rotated focal mechanism, whereas 14 are located either within or to the southwest of the first patch of moment release (Figure 12). Also, the outlying aftershock to the northeast is located nearest to a patch of moment release showing an intermediate focal mechanism (strike 5°), not the final one showing the largest fault rotation. So it is natural that the well-located aftershocks show the best fit to the focal mechanism of the first subevent.

The observation that the focal mechanism of the rupture changed suddenly as the rupture propagated beyond the limits of the seismically active zone suggests that the region surrounding this zone is characterized by a different ambient stress field than the slab core, where the rupture initiated. If the material surrounding slabs is generally characterized by different stress fields from the slab core, it may provide an explanation for the observation that large deep earthquakes have larger non-double-couple components than smaller events [*Houston,* 1993]. If the largest deep earthquakes generally encounter different ambient stress fields when they propagate outside the slab core, they may be characterized by the sort of focal mechanism change (and probable fault curvature) that is observed for the Tonga event. Since curved fault surfaces and changes in focal mechanism are a probable cause of non-double-couple components [*Frohlich,* 1994; 1990], this effect may cause large deep earthquakes to show larger non-double-couple components than small events, in which the entire rupture would occur within the slab core.

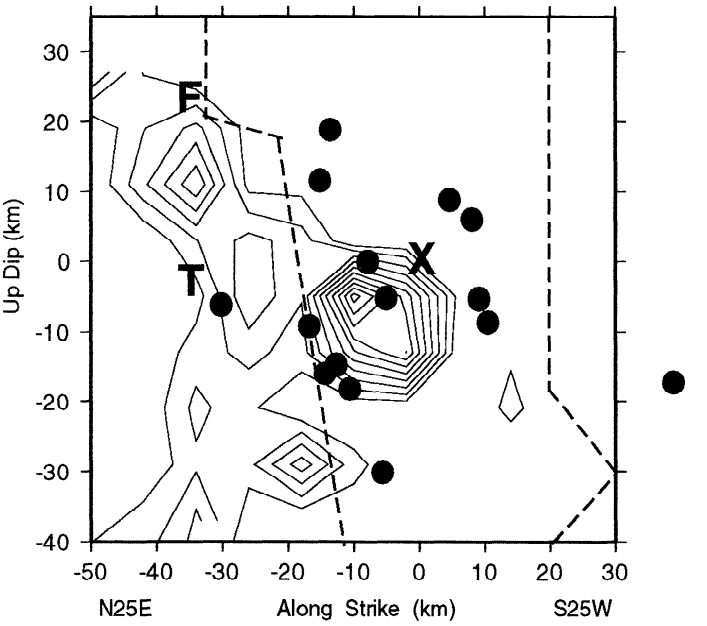

Figure 12. A view of the moment release and aftershock locations along the vertical fault plane (strike 30°, dip 65°) for the lowest error waveform inversion solution (rupture velocity is 4.1 km/s). The slip contours have a contour interval of 0.5m. The view is from the northwest, perpendicular to the fault plane. The location of the edges of the background seismicity (Plate 3) are plotted as dashed lines, the hypocenter is denoted with a cross, the aftershocks are denoted as dots, and the location of the end of the rupture as determined by the directivity analysis is plotted as a T. The location of the March 2 foreshock is plotted as a F. The rupture initiated in the interior of the previously seismically active zone and proceeded to the northeast, extending about 15-20 km beyond the edge of the previously active seismic zone. Aftershocks are concentrated in the previously active slab core in regions of low seismic moment release adjacent to the first subevent. Aftershocks seem to be suppressed in the outer, previously aseismic regions of the rupture, which contain half the moment release but only one of 15 well-located aftershocks. The inversion results suggest there was no significant slip at the location of the outlying aftershock to the southwest.

Stress Drop and Rupture Velocity

We calculated the average stress drop for the moment release distribution shown in Plate 2a using the relationship for a circular

fault of *Kanamori and Anderson* [1975]. We calculated the total area of all the subfaults with slip magnitudes above a cutoff level and used this and the moment of the March 9 event to determine the average stress drop. For a slip cutoff of 0.5 m (corresponding to a total area of 1540 km^2), the average stress drop is 13 MPa (130 bars). This is higher than the value we reported previously (1.6 MPa) [*Wiens et al.,* 1994], based solely on the size of the aftershock distribution which is much larger than the rupture area found by our waveform inversion, largely due to the absence of any slip between the hypocenter and the outlying aftershock to the southwest.

The stress drop of the Tonga event is still close to the range of stress drops generally found for shallow earthquakes (1-10 MPa) [*Kanamori and Anderson*, 1975] and much smaller than stress drops of 114 MPa [*Lundgren and Giardini*, 1995], 283 MPa [*Goes and Ritsema*, 1995], and 110 MPa [*Kikuchi and Kanamori*, 1994] found for the 1994 Bolivia earthquake. The rupture velocity that we find for the 1994 Tonga event (about 4.1 km/s) is also much different from the slow rupture velocity of 1-2 km/s found for the Bolivia event [*Beck et al.*, 1995], suggesting fundamental differences in the rupture properties between these large deep events [*Wiens and McGuire*, 1995].

Discussion

Rupture Outside the Previously Active Seismic Zone

This study is the first detailed mapping of a moment release along a deep earthquake fault plane in an area where both the orientation of the slab and the normal extent of the seismogenic zone are known. The rupture zone is clearly shown to extend beyond the limits of the background slab seismicity. Plate 3 shows a cross-sectional view of the region of the Tonga slab where the March 9th event occurred. The background seismicity (shown in blue) in this region forms an indistinct double seismic zone that is about 30-35 km wide in the region of the main shock and somewhat wider (40-45 km) about 50 km shallower. The main shock hypocenter is located in the center of the previously active zone. The rupture ended about 15 km (from the directivity study) to 20 km (from the waveform inversion) to the northeast of the edge of the background seismicity. The most significant uncertainty in this conclusion is the delineation of the previously active seismic zone; the current figure includes 170 earthquakes from 1980 to 1995 and indicates that no earthquakes occurred in this region prior to the March 2 foreshock. This confirms previous suggestions, based on aftershock locations for the Tonga event [*Wiens et al.,* 1994] and the width of the deep earthquake rupture zone of the 1994 Bolivia earthquake [*Silver et al.*, 1995; *Beck et al.*, 1995], that the rupture zones of large deep earthquakes are not confined to a narrow region in the cold core of the slab, as might be expected from the transformational faulting model of deep earthquakes [*Green and Burnley*, 1989; *Kirby et al.*, 1991].

However, the current result provides stronger constraints on deep earthquake processes, since the extent of the rupture can be clearly determined relative to the known width of the previously active seismic zone. In addition, the location of the pulses of moment release of a deep earthquake can be compared to aftershock locations for the first time. In the following sections, we discuss the significance of the rupture characteristics of the Tonga event for models of deep earthquakes.

Slip Distribution and Aftershock Occurrence

The larger, well-located aftershocks of the March 9 event are not evenly distributed with respect to the rupture area found in our waveform inversion. Figure 12 shows the distribution of aftershocks on the vertical fault plane, and the boundaries of the zone in which background seismicity normally is observed (see Plate 3). Most of the aftershocks are distributed within the zone of background seismicity which presumably represents the cold slab core, generally located within regions of low moment release immediately adjacent to the first main pulse of moment release. Such clustering around the edges of the rupture has been observed in shallow earthquake aftershock sequences [*Mendoza and Hartzell*, 1988; *Houston and Engdahl*, 1989; *Beroza*, 1991] and may be due to stress concentrations around the edge of the rupture resulting from the slip of the main shock. However, it also appears that aftershocks are suppressed in the regions of high moment release outside the active seismic zone. Although about half of the moment release occurs within the previously aseismic region to the northeast of the seismically active slab core, only one of the 15 well-located aftershocks is located here.

The outlying aftershock to the southwest (March 10, 1994 14:08 UT) occurred in a region where the inversion found no slip. Although this region is off the edge of the slip map displayed in Figure 12, it showed no slip when the region of solution was extended to include the aftershock. For there to be significant slip at the location of this aftershock, a rupture velocity of greater than 5.5 km/s would be required to be compatible with the short durations observed at stations to the northeast. This velocity is equal to the shear wave velocity at this depth. Thus we conclude that this aftershock lies outside the region of significant moment release during the main shock, although it lies along the extension of the fault plane. Isolated aftershocks from shallow earthquakes are commonly found at considerable distance from the regions of significant moment release during the mainshock [*Mendoza and Hartzell*, 1988].

The rupture appears to have terminated just beneath and to the north of the a small forshock that occurred 1 week prior to the mainshock, in a region of no prior seismicity [D. A. *Wiens et al.,* manuscript in preparation, 1997]. The outer shallowest edge of the rupture may include the location of the foreshock, and the location of the foreshock may have been significant in localizing the rupture in this region.

The Relationship Between Slip Distribution and Slab Thermal Structure

It is presumed that the localization of deep earthquakes within subducting slabs results from the fact that the slabs represent a thermal anomaly relative to the surrounding mantle. It has also been observed that there is a critical thermal parameter below which subducted slabs do not show deep earthquakes, indicating that deep earthquakes do not occur in warm slabs [*Kirby et al.*, 1991]. These two concepts suggest that deep earthquake faulting, regardless of the mechanism, can only occur in material which is cooler than a certain critical temperature. We modeled the thermal structure of the subducting Tonga slab using the finite difference method of *Toksoz et al* [1973]. Thermal modeling of this part of the Tonga slab is complicated for a number of reasons. The slab bends from a dip of 45° between 300-450 km depth to a near-vertical dip at depths greater than 500 km. This bend probably separates slab material subducted before and after

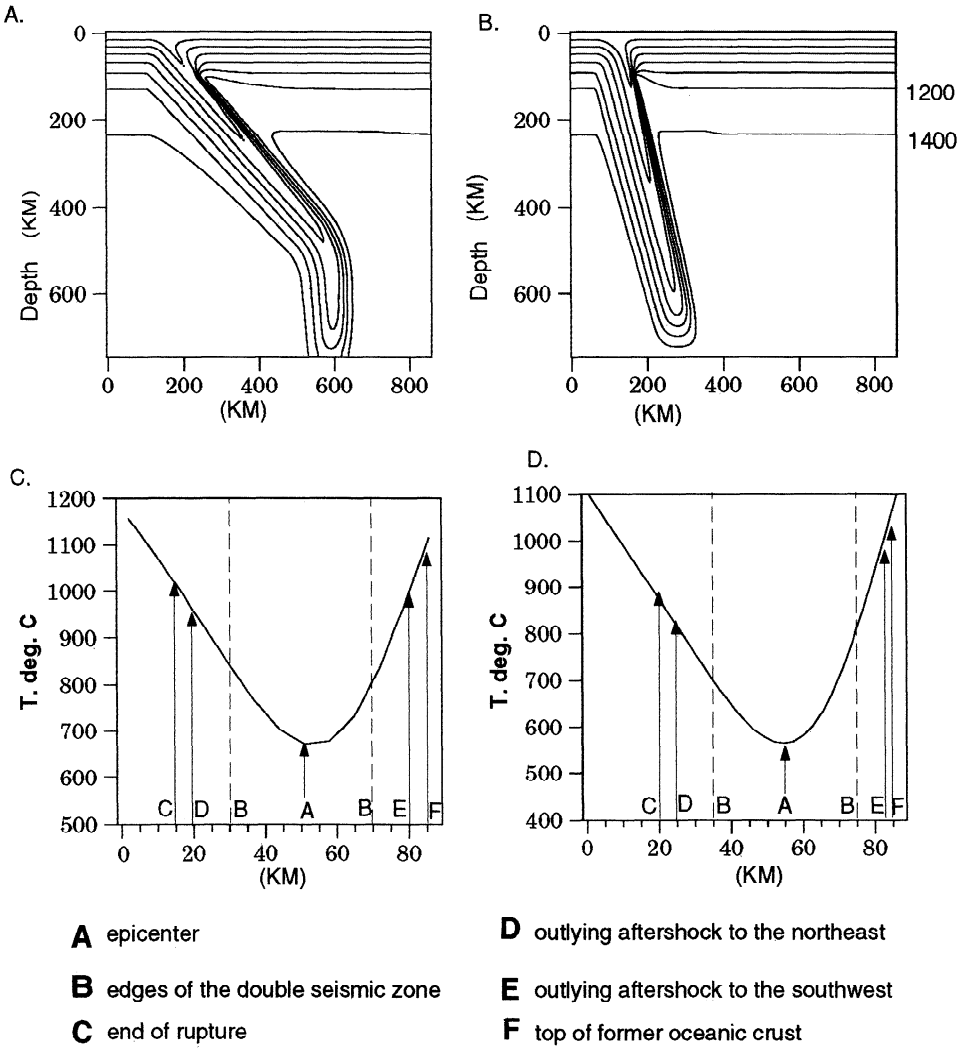

Figure 13. Models used to estimate temperatures in the Tonga slab at the depth of the March 9 event. There is considerable uncertainty about the thermal model for the lower Tonga slab, since it is likely that no steady state model adequately reproduces the complex subduction history. Model A represents a warm end-member model, assuming an approximately steady state slab in its present geometry (becoming vertical at about 500 km depth) and a convergence velocity of 10 cm/yr relative to the mantle. A cold end-member thermal model (model B) proposes that the material near the March 9 event descended on a nearly vertical paleosubduction zone geometry at a velocity of 12 cm/yr. Figures 13c and 13d are profiles across the slab at 565 km depth for the two models. Although the actual temperatures of various features vary considerably between the models, the gradient between the limit of the background seismicity and the termination of the March 9 rupture is approximately 11° to 14°C/km in both cases. This suggests that the rupture terminated in material about 200°C warmer than the normal limiting temperature of seismicity.

the onset of rapid backarc opening in the Lau basin [*Hamburger and Isacks*, 1988]. Thus the subduction geometry of the Tonga zone probably represents a changing dynamic system not readily modeled using steady state thermal models. The velocity at which the subducted plate is moving relative to the mantle is also uncertain because of the large component of the Tonga trench convergence rate caused by trench roll back. The convergence velocity at the Tonga trench is estimated at about 20 cm/yr from Global Positioning System (GPS) measurements [*Bevis et al.*, 1995], but some of this velocity probably represents trench roll back and not actual motion of the deep slab with respect to the deep mantle. The absolute velocity of the Pacific plate relative to the hotspots in this region (10.6 cm/yr) [*Minster and Jordan*, 1978; *Gripp and Gordon*, 1990] probably represents a better estimate of the time-averaged penetration velocity of the deep slab with respect to the mantle.

To help bracket the probable thermal structure at the location of the March 9 event, we investigated two end-member scenarios. The first is that the slab material near the March 9 event actually descended nearly vertically through the mantle and that the steep dip of the slab at this depth is a remnant feature from a previously near-vertical slab. This model represents a cold end-member geometry, and we assign it a faster convergence rate of 12 cm/yr. The other end-member model assumes that the present geometry represents a steady state geometry and has the slab descending at a 45° dip until about 500 km depth where it then bends to a dip of 90°. We assign this hot end-member model a convergence velocity of 10 cm/yr. The lithosphere is

assumed to have a thermal gradient given by a half space thermal model appropriate for a lithospheric age of 100 Ma prior to subduction. The two end-member models of the subduction history shown in figures 13a and 13b give an approximate range of possible thermal structures. Figure 13c and 13d show horizontal temperature profiles across the respective models at the depth of the March 9th event. Assuming that the center of the active seismic zone represents the coldest part of the slab, the features of the March 9th rupture can be mapped onto the thermal profiles. Although the temperature of the various features varies between the models, the gradient between the northeastern edge of the active seismic zone and the rupture termination point is roughly constant. This region shows thermal gradients of 11°-14°C/km for a wide range of possible thermal models that we have tested, including the two end-member models shown here. This thermal gradient suggests that the rupture termination point occurred in material that is about 200° warmer than the temperature which limits rupture initiation of moderate sized events, a conclusion that is relatively robust with respect to different possible thermal models.

Thus the March 9 rupture propagated through previously aseismic material until it reached temperatures that are about 200° warmer than the normal limiting temperature of deep seismicity in the slab. The region near the end of the rupture to the NE has very different faulting properties than the slab core in which seismicity normally initiates. It shows no background seismicity, and aftershock production relative to moment release seems to be suppressed by about an order of magnitude, as discussed above. This suggests that while the outer region of the slab is able to sustain rupture, it is not capable of initiating moderate size ruptures and aftershocks are generated only with difficulty. This suggests that slabs may be composed of a cold core, where seismic rupture initiates and small earthquakes occur, and a thermal "halo" of warmer material, which can sustain rupture, but few smaller earthquakes, and where aftershocks are generated only with difficulty during transient processes following very large earthquakes.

Implications for the Mechanism of Deep Earthquakes

Does the Tonga event represent a reactivated fault? The two large deep earthquakes of 1994 have focused attention on the size of deep earthquake faults. The Bolivia event requires the faulting and aftershock zone to be at least 35 km wide in the direction perpendicular to the slab [*Beck et al.*, 1995; *Silver et al.*, 1995], while the Tonga event requires this zone to be at least 60 km wide. These widths are larger than any estimate of the metastable olivine wedge thickness for the respective slabs. This observation led Silver et al. [1995] to reject the transformational faulting hypothesis and to propose the reactivation of trench parallel normal faults as an explanation of large deep earthquakes. This model is not compatible with the Tonga event for two reasons. First, the orientation of the 1994 Tonga earthquake fault crosscuts the subducting Tonga slab at a high angle. Reconstructing the position of the fault plane of the Tonga event at either the present-day Tonga subduction zone or the relict Vitiaz Trench [*Hamburger and Isacks*, 1987] demonstrates that the Tonga fault would have represented a nearly vertical fault oriented nearly perpendicular to the trench strike. Thus the 1994 Tonga fault could not have been formed by a typical outer rise earthquake, which generally strike parallel to the trench. Second, if the rupture of the Tonga event is assumed to be limited to the preexisting fault plane, the fault must have extended to a depth of at least 60 km below the surface. Most earthquakes in oceanic lithosphere are limited to depths of less than 40 km [*Wiens and Stein*, 1983]. Faulting has not been conclusively shown to extend depths greater than about 40 km even for the largest lithospheric faulting events [*Lynnes and Lay*, 1988]. Although a reactivation of some unknown and arbitrary fault cannot be ruled out, the characteristics of the 1994 Tonga event are not consistent with those expected of typical faults likely to be located in the subducted lithosphere.

Two different faulting Regimes for deep earthquakes. The 1994 Tonga earthquake demonstrates that the process of deep earthquake rupture propagation is stable to higher temperatures and occurs over larger distances from the slab core than the normal process of earthquake nucleation. This implies that theories of deep earthquake initiation that require a thin zone of earthquake nucleation, like transformational faulting or dehydration within a thin hydrated region, are still possible. However, another mechanism must be found to explain rupture propagation and the nucleation of a small number of aftershocks within the higher-temperature thermal halo surrounding the slab core.

We propose that once a large earthquake is nucleated within the slab core, transient processes resulting from the growing rupture allow the propagation to continue into regions which are normally incapable of nucleating earthquakes. The rupture could propagate through hotter material by a ductile faulting [*Hobbs and Ord*, 1988] or a shear instability mechanism [*Ogawa*, 1987], in which the temperature increase caused by the developing rupture at the rupture tip allows the fault to propagate. Transient processes surrounding this outer rupture region may allow isolated aftershocks during the first few weeks following the main shock, but aftershock occurrence in this region is also suppressed relative to the part of the rupture within the slab core. The observations of the 1994 Tonga earthquake and its relation to the Tonga subduction zone are entirely consistent with two distinct regimes of faulting. One regime is operative in the cold core of the slab in which earthquakes nucleate, perhaps due to transformational faulting, and where moderate size earthquakes and aftershocks are concentrated. A distinct outer regime is operative in the warmer regions surrounding the slab core up to temperatures about 200°C greater than the limiting temperature of the smaller earthquakes. This region is generally not capable of initiating earthquakes, except as a very limited number of aftershocks following the penetration of this region by the rupture zone of a very large earthquake.

This analysis of the 1994 Tonga rupture may have important implications for understanding the differences between large deep earthquakes. It is interesting to note that the seismological characteristics of the material at the termination point of the Tonga rupture is similar to that of the very largest deep earthquakes, such as the 1970 Columbia event or the 1994 Bolivia event. These events generally occur in isolated regions, showing little or no background seismicity and very few aftershocks [*Wiens and McGuire*, 1995]. We propose that these seismological characteristics are thermal effects, caused by the location of these events in regions that are too warm to sustain normal seismic activity. The very largest deep events generally occur in warmer slabs or isolated regions, where temperatures may be similar to the rupture termination point in Tonga. For example, thermal models for the region of the 1994 Bolivia event suggest slab temperatures of around 750°-900°C, similar to those inferred for the outer portions of the Tonga rupture (Figure 13). Such events may be triggered on rare occasions, perhaps by

transformational faulting within very small pockets of residual metastable olivine, and propagate outside the rupture initiation zone by the same process observed in Tonga.

Conclusions

The March 9th 1994, deep Tonga event provides the best opportunity to date to map the rupture area of a large deep earthquake relative to a well-defined Benioff zone. The background seismicity in this region forms a 30-40 km wide planar region with well-defined limits. Rupture initiated in the core of this zone and propagated to the northeast, extending 15-20 km beyond the limits of background seismicity. If the background seismicity zone is assumed to be the cold core of the slab, features of the March 9 rupture can be related to thermal models. A wide range of thermal models show a nearly constant gradient between the edge of the background seismicity and the location of the end of the rupture. This gradient suggests that the rupture terminated in material which is 100-300°C warmer than the temperature which limits rupture initiation. Despite at least half of the moment release occurring beyond the seismically active core of the slab, only one of 15 well-located aftershocks is found in this region. The outer region of the slab is able to sustain rupture, but it is not capable of initiating rupture, and aftershocks are generated only with difficulty. Our observations suggest that the process of deep earthquake rupture is stable to about 200°C warmer temperatures than the process of deep earthquake initiation. We propose that there are two distinct faulting regimes for deep earthquakes, one in the slab core where earthquakes nucleate, and another within the surrounding warmer region, which can only sustain rupture during transient events within and immediately following very large, deep earthquakes.

Acknowledgments. We thank Paul Friberg (PASSCAL Instrument Center), George Hade (Cornell), Kiti Draunidalo (Fiji MRD), Simone Helu (Tonga Ministry of Lands), and George Sionihalo (Niue Department of Survey) for assistance in deploying the seismographs. Instruments for this study were obtained from the PASSCAL program of IRIS (Incorporated Research Institutions in Seismology), and teleseismic data were obtained from the IRIS Data Management Center. This manuscript was improved by reviews from C. Frohlich, H. Houston, and an anonymous reviewer. This research was supported by the National Science Foundation under grants EAR 9219675 and EAR9418942.

References

Ammon, C. J., and J.E., Vidale, Tomography without rays, *Bull. Seismol. Soc. Am.*, *83*, 509-528, 1993.

Ammon, C. J., A. A. Velasco, and T. Lay, Rapid estimation of rupture directivity: Application to the 1992 Landers (Ms=7.4) and Cape Mendocino (Ms=7.2) California Earthquakes, *Geophys. Res. Lett.*, *20*, 97-100, 1993.

Antolik, M., D. Dreger, and B. Romanowicz, Empirical Green's function source analysis of the large deep focus Fiji and Bolivian earthquakes of 1994, *Eos Trans. AGU.*, *75*(44), Fall Meet. Suppl. 468, 1994.

Beck, S.L., P. Silver, T.C. Wallace, and D. James, Directivity analysis of the deep Bolivian earthquake of June 9, 1994, *Geophys. Res. Lett.*, *22*, 2257-2260, 1995.

Beroza, G. C., Near source modeling of the Loma Prieta Earthquake: Evidence for heterogeneous slip and implications for earthquake hazard, *Bull. Seismol. Soc. Am.*, *81*, 1603-1621, 1991.

Bevis, M. G., F. W. Taylor, B. E. Schutz, J. Recy, B. L. Isacks, S. Helu, R. Singh, E. Kendrick, J. Stowell, B. Taylor, and S. Calmant, Geodetic observations of very rapid convergence and back-arc extension at the Tonga arc, *Nature*, *374*, 249-251, 1995.

Chung, W.-Y., and H. Kanamori, Source process and tectonic implications of the Spanish deep-focus earthquake of March 29, 1954, *Phys. Earth Planet. Inter.*, *13*, 85-96, 1976.

Dreger, D.S., Empirical Green's function study of the January 17, 1994 Northridge, California earthquake, *Geophys. Res. Lett.*, *21*, 2633-2636, 1994.

Dziewonski, A. M., G. Ekstrom, M. P. Salganick, Centroid-Moment Tensor Solutions for January - March 1994, Phys. Earth Planet. Inter., *86*, 253-261, 1994.

Flinn, E.A., Confidence regions and error determination for seismic event location, *Rev. Geophys.*, *3*(1), 157-185, 1965.

Frohlich, C., The nature of deep-focus earthquakes, *Annu. Rev. Earth Planet. Sci.*, *17*, 227-254, 1989.

Frohlich, C., Note concerning non-double-couple source components from slip along surfaces of revolution, *J. Geophys. Res.*, *95*, 6861-6866, 1990.

Frohlich, C., Earthquake with non-double-couple mechanisms, *Science*, *264*, 804-809, 1994.

Fukao, Y., and M. Kikuchi, Source retrieval for mantle earthquakes by iterative deconvolution of long-period *P* waves, *Tectonophysics*, *144*, 249-269, 1987.

Furumoto, M., Spacio-temporal history of the deep Colombia earthquake of 1970, *Phys. Earth Planet. Inter.*, *15*, 1-12, 1977.

Glennon, M., and W.-P. Chen, Ruptures of deep-focus earthquakes in the northwestern Pacific and their implications on seismogenesis, *Geophys. J. Int.*, *120*, 706-720, 1995.

Goes, S., and J. Ritsema, A broadband *P* wave analysis of the large deep Fiji Island and Bolivia earthquakes of 1994, *Geophys. Res. Lett.*, *22*, 2249-2252, 1995.

Green, H.W., and P.C. Burnley, A new self-organizing mechanism for deep focus earthquakes, *Nature*, *341*, 733-737, 1989.

Gripp, A.E., and R.G. Gordon, Current plate velocities relative to the hotspots incorporating the NUVEL-1 global plate motion model, *Geophys. Res. Lett.*, *17*, 1107-1112, 1990.

Hamburger, M.W., and B.L. Isacks, Deep earthquakes in the southwest Pacific: A tectonic interpretation, *J. Geophys. Res.*, *92*, 13,841-13,854, 1987.

Hamburger, M.W., and B.L. Isacks, Diffuse back-arc deformation in the southwestern Pacific, *Nature*, *332*, 599-604, 1988.

Hobbs, B.E., and A. Ord, Plastic Instabilities: Implications for the origin of intermediate and deep focus earthquakes, *J. Geophys. Res.*, *93*, 10,521-10,540, 1988.

Hogrefe, A., D. C. Rubie, T. G. Sharp, and F. Seifert, Metastability of enstatie in deep subducting lithosphere, *Nature*, *372*, 351-353, 1994.

Houston, H., The non-double-couple component of deep earthquakes and the width of the seismogenic zone, *Geophys. Res. Lett.*, *20*, 1687-1690, 1993.

Houston, H., and E.R. Engdahl, A comparison of the spatio-temporal distribution of moment release for the 1986 Andreadnof Islands earthquake with relocated seismicity, *Geophys. Res. Lett.*, *16*, 1421-1424, 1989.

Jordan, T.H., and K.A. Sverdrup, Teleseismic location techniques and their application to earthquake clusters in the south-central Pacific, *Bull. Seismol. Soc. Am.*, *71*, 1105-1130, 1981.

Kanamori, H., and D.L. Anderson, Theoretical basis of some empirical relations in seismology, *Bull. Seismol. Soc. Am.*, *65*, 1073-1095, 1975.

Kanamori, H., and G.S. Stewart, Mode of the strain release along the Gibbs Fracture Zone, Mid-Atlantic Ridge, *Phys. Earth Planet. Inter.*, *11*, 312-332, 1976.

Kikuchi, M., and Y. Fukao, Iterative deconvolution of complex body waves from great earthquakes - The Tokachi-Oki earthquake of 1968, *Phys. Earth Planter. Inter.*, *37*, 235-248, 1985.

Kikuchi, M., and H. Kanamori, Inversion of complex body waves 3, *Bull. Seismol. Soc. Am.*, *81*, 2335-2350, 1991.

Kikuchi, M., and H. Kanamori, The mechanism of the deep Bolivian earthquake of June 9, 1994, *Geophys. Res. Lett.*, *21*, 2341-2344, 1994.

Kirby, S.H., W.B. Durham, and L.A. Stern, Mantle phase changes and deep-earthquake faulting in subducting lithosphere, *Science*, *252*, 216-225, 1991.

Kjartansson, E., Constant Q-wave propagation and attenuation, *J. Geophys. Res. 84*, 4737-4748, 1979.

Lawson C.L., and R.J. Hanson, *Solving Least Squares Problems*, Prentice-Hall, Englewood Cliffs N. J., 1974.

Leith, A., and J.A. Sharpe, Deep focus earthquakes and their geological significance, *J. Geol. 44*, 877-917, 1936.

Lundgren, P., and D. Giardini, The June 9 Bolivia and March 9 Fiji deep earthquakes of 1994, I, Source processes, *Geophys. Res. Lett., 22*, 2241-2244, 1995.

Lynnes, C.S., and T. Lay, Source process of the great 1977 Sumba earthquake, *J. Geophys. Res., 93*, 13,407-13,420, 1988.

Meade, C., and R. Jeanloz, Deep-focus earthquakes and recycling of water into the Earth's mantle, *Science, 252*, 68-72, 1991.

Mendoza, C., and S. H. Hartzell, Aftershock patterns and main shock faulting, *Bull. Seismol. Soc. Am., 78*, 1438-1449, 1988.

Menke, W., *Geophysical Data Analysis: Discrete Inverse Theory*, Academic, San Diego, Calif., 1989.

Minster, J.B., and T.H. Jordan, Present-day plate motions, *J. Geophys. Res., 83*, 5331-5354, 1978.

Mori, J., and S. Hartzell, Source Inversion of the 1988 Upland earthquake: Determination of a fault plane for a small event, *Bull. Seismol. Soc. Am., 80*, 507-518, 1990.

Ogawa, M., Shear instability in a visco-elastic material as the cause of deep focus earthquakes, *J. Geophys. Res., 92*, 13,801-13,810, 1987.

Roth, E., M. P. Flanagan, D. A. Wiens, P. J. Shore, and M. G. Bevis, Attenuation structure of the Lau back arc from regional broadband waveforms, *Eos Trans. AGU, 75*(44), Fall Meet. Suppl., 450, 1994.

Silver, P. G., S. L. Beck, T. C. Wallace, C. Meade, S. C. Myers, D. E. James, and R. Kuehnel, Rupture characteristics of the deep Bolivian earthquake of 9 June 1994 and the mechanism of deep-focus earthquakes, *Science, 268*, 69-73, 1995.

Toksoz, M.N., N.H. Sleep, and A.T. Smith, Evolution of the downgoing lithosphere and the mechanisms of deep focus earthquakes, *Geophys. J. R. Astron. Soc., 35*, 285-310, 1973.

Wiens, D. A., and J. J. McGuire, The 1994 Bolivia and Tonga events: Fundamentally different types of deep earthquakes?, *Geophys. Res. Lett., 22*, 2245-2248, 1995.

Wiens, D.A., and S. Stein, Age dependence of oceanic intraplate seismicity and implications for lithospheric evolution, *J. Geophys. Res., 88*, 6455-6468, 1983.

Wiens, D.A., J.J. McGuire, and P.J. Shore, Evidence for transformational faulting from a deep double seismic zone in Tonga, *Nature, 364*, 790-793, 1993.

Wiens, D. A., J. J. McGuire, P. J. Shore, M. G. Bevis, K. Draunidalo, B. Prasad, and S. P. Helu, A deep earthquake aftershock sequence and implications for the rupture mechanism of deep earthquakes, *Nature, 372*, 540-543, 1994.

Wiens, D. A., P. J. Shore, J. J. McGuire, E. Roth, M. Bevis, and K. Draunidalo, The Southwest Pacific Seismic Experiment, *IRIS Newsl., 14*, 1-4, 1995.

Willemann, R.J., and C. Frohlich, Spatial patterns of aftershocks of deep focus earthquakes, *J. Geophys. Res., 92*, 13,927-13,943, 1987.

Yoshida, S., Waveform inversion for rupture processes of two deep earthquakes in the Izu-Bonin region, Waveform inversion for rupture process of two deep earthquakes in the Izu-Bonin region, *Phys. Earth Planet. Inter., 52*, 85-101, 1988.

M. G. Bevis, Hawaii Institute of Geophysics, University of Hawaii, 2525 Correa Road, Honolulu, HI, 96822. (e-mail: bevis@soest.hawaii.edu)

J. J. McGuire, Department of Earth, Atmospheric, and Planetary Sciences, Massachusetts Institute of Technology, 77 Massachusetts Ave., Cambridge, MA 02139, (e-mail: jeff@quake.mit.edu)

P. J. Shore and D. A. Wiens, Department of Earth and Planetary Sciences, Washington University, One Brookings Dr. Box 1169, St. Louis MO 63130. (e-mail: patrick@wups.wustl.edu; doug@kermadec.wustl.edu)

(Received December 4, 1995; revised October 1, 1996;
accepted October 11, 1996.)